



CUBESAT ATTITUDE DETERMINATION
AND HELMHOLTZ CAGE DESIGN

THESIS

Megan R. Brewer, Captain, USAF

AFIT/GAE/ENY/12-M03

DEPARTMENT OF THE AIR FORCE
AIR UNIVERSITY

AIR FORCE INSTITUTE OF TECHNOLOGY

Wright-Patterson Air Force Base, Ohio

APPROVED FOR PUBLIC RELEASE; DISTRIBUTION UNLIMITED

The views expressed in this thesis are those of the author and do not reflect the official policy or position of the United States Air Force, Department of Defense, or the United States Government. This material is declared a work of the U.S. Government and is not subject to copyright protection in the United States.

AFIT/GAE/ENY/12-M03

CUBESAT ATTITUDE DETERMINATION AND HELMHOLTZ CAGE DESIGN

THESIS

Presented to the Faculty

Department of Aeronautics and Astronautics

Graduate School of Engineering and Management

Air Force Institute of Technology

Air University

Air Education and Training Command

In Partial Fulfillment of the Requirements for the
Degree of Master of Science in Aeronautical Engineering

Megan R. Brewer, B.S. Aerospace Engineering

Captain, USAF

March 2012

APPROVED FOR PUBLIC RELEASE; DISTRIBUTION UNLIMITED

CUBESAT ATTITUDE DETERMINATION AND HELMHOLTZ CAGE
DESIGN

Megan R. Brewer, B.S. Aerospace Engineering
Captain, USAF

Approved:



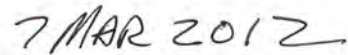
Dr. Eric D. Swenson (Chairman)



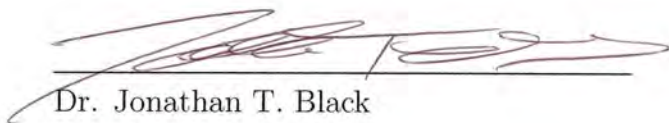
Date



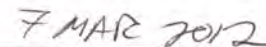
Dr. Richard G. Cobb



Date



Dr. Jonathan T. Black



Date

Abstract

A method of 3-axis satellite attitude determination utilizing six body-fixed light sensors and a 3-axis magnetometer is analyzed. A Helmholtz cage is designed, built, and tested to provide a dynamic, 3-axis, uniform magnetic field to cancel the Earth's magnetic field and create an environment similar to the geomagnetic field a satellite would experience on-orbit. A CubeSat is provided the inertial magnetic vector and "Sun" vector which are combined with data from the light sensors and magnetometer in a CubeSat. Attitude is estimated on-board the CubeSat via the optimal fast quaternion estimation algorithm. The capabilities of the Helmholtz cage including the uniformity of the produced magnetic field are examined as well as the accuracy of the on-board attitude determination. The results show that a support column in the vicinity of the cage impacts the uniformity of the magnetic field. The desired ± 2 Gauss magnetic field was achieved in two of three directions and the cage is equipped to simulate a dynamic magnetic field as would be experienced in orbit. Attitude determination with the OFQEA is achieved to within $\pm 6^\circ$ of error.

Acknowledgements

First, I would like to thank the ENY department and specifically my thesis advisor Dr. Swenson for letting me take on this research, guiding me along the path, and asking the tough questions even when I didn't want to hear them. Without his guidance and support I would not have been able to achieve even half of the work involved in this research effort.

I would also like to thank Chris Zickefoose for helping me by ordering parts, designing the corners and coil supports, and guiding me on how to work with the materials. Thank you to Sean Miller and Jeremy Kaczmarek for their suggestions and guidance specifically on the electrical portion of this research. Thank you to the guys down at the machine shop for their willingness to machine the corners and coil supports with little notice. The work performed at the machine shop was vital to this design just as the machine shop is an absolute asset to AFIT.

Thank you to the personnel at the Naval Post Graduate School, the University of Michigan, and the Delft University of Technology for always answering my emails when I had questions, sharing pictures of their design, and sharing any documentation on their Helmholtz cage design. All three schools have helped to shape the design of the AFIT Helmholtz cage.

I also have my classmates and good friends to thank for helping wrap the coils and install them in the cage, with or without my bribery of baked goods. I would still be wrapping the coils without the aid of others. Finally, thank you to my family for the words of encouragement and the continual patience provided throughout this process. You gave me the strength to make it through this challenging, but very rewarding, research.

Megan R. Brewer

Table of Contents

	Page
Abstract	iii
Acknowledgements	iv
List of Figures	viii
List of Tables	x
 I. Introduction	 1
1.1 Background	1
1.2 Problem Statement	2
1.3 Research Focus	3
1.4 Methodology	4
1.5 Preview	5
 II. Background	 7
2.1 Simulated Satellites	7
2.2 Attitude Sensors	8
2.3 Geomagnetic Field	13
2.3.1 Magnetosphere and Ionosphere	16
2.3.2 Geomagnetic Models	18
2.4 Helmholtz Coils	19
2.5 Helmholtz Cages	22
2.5.1 MEDA, Inc. Helmholtz Cage	23
2.5.2 Delft University of Technology Helmholtz Cage	24
2.5.3 University of Michigan Helmholtz Cage	26
2.6 Attitude Determination	29
2.6.1 Deterministic Attitude Determination	29
2.6.2 Optimal Attitude Determination	31
2.7 Summary	36
 III. Methodology	 37
3.1 Introduction	37
3.2 Cage Design	37
3.3 Cage Equipment	42
3.3.1 Power Supplies	42
3.3.2 Truth Magnetometer	42
3.3.3 Light Source	42
3.3.4 Test Stand	43

	Page
3.3.5 Relays	43
3.3.6 Control Computer	44
3.4 Cage Control with STK	44
3.5 Cage Test Setup	47
3.5.1 Object Influence on Magnetic Field	47
3.5.2 Room Survey	47
3.5.3 Expected Generated Magnetic Field	48
3.5.4 Zeroing the Ambient Magnetic Field	49
3.6 CubeSat Components	49
3.6.1 Sun Sensors	50
3.6.2 Magnetometer	51
3.7 CubeSat Attitude Determination Algorithm and Testing	53
3.8 Summary	56
IV. Results & Analysis	57
4.1 Analysis of Ambient Magnetic Field Pre-Cage	57
4.1.1 Effects of Electrical and Ferromagnetic Objects	57
4.1.2 Room Survey	58
4.2 Helmholtz Cage Analysis	60
4.2.1 Resultant Magnetic Field Capability	60
4.2.2 Zeroing the Ambient Magnetic Field	62
4.2.3 Dynamic Cage Control with STK	68
4.3 On-board Magnetometer Analysis	70
4.3.1 Magnetometer Linearity	70
4.3.2 Reaction Wheel Effects on On-board Magnetometer	72
4.3.3 Magnetometer Offset	73
4.4 CubeSat Attitude Determination	75
4.4.1 OFQEA Testing with Magnetic Field in $-Z_i$	75
4.4.2 OFQEA Testing with Magnetic Field in Y_i	77
4.4.3 Optimal Method vs. TRIAD	80
4.5 Summary	81
V. Conclusions and Recommendations for Future Development	83
5.1 Summary	83
5.2 Conclusions	84
5.3 Recommendations for Future Development	86
5.3.1 Finalizing the Cage	86
5.3.2 Attitude Determination	87
5.4 Future Applications of the Helmholtz Cage	88

	Page
Bibliography	89

List of Figures

Figure		Page
1.1	AFIT's Helmholtz Cage with Test CubeSat and Test Stand at Center	4
1.2	Expanded View of Test CubeSat	5
2.1	CubeSat Reference Frame Unit Vectors with Sun	9
2.2	Representation of Earth's Magnetic Field [1]	14
2.3	Earth's Core [2]	14
2.4	Earth's Ionosphere and Magnetosphere - (not drawn to scale) [3] .	16
2.5	Diurnal Variations at Select Observatories [4]	17
2.6	Helmholtz Coil Pair [5]	20
2.7	Uniform Field for Circular Coils [5]	20
2.8	Magnetic Field Uniformity for a Circular Coil [6]	21
2.9	Square Helmholtz Coil Pair ©IEEE [7]	22
2.10	MEDA Helmholtz Cage [8]	24
2.11	Delft University of Technology Cages [9]	25
2.12	University of Michigan's Helmholtz Cage [10]	27
2.13	Magnetic and Sun Vectors in the Body and Inertial Reference Frames	30
3.1	Estimated Uniformity of Generated Magnetic Field	38
3.2	Corner Piece Components	38
3.3	Coil Wrapping Configuration	40
3.4	AFIT Helmholtz Cage	41
3.5	Test Stand	43
3.6	Closed-Loop Control of the Magnetic Field	45
3.7	Three Magnetometer System	48
3.8	Test Plane	49
3.9	TEMT6000 Light Sensor	50
3.10	Sun Vector Angles in the CubeSat Reference Frame	51
3.11	Sparkfun 9 DOF Board	52

Figure		Page
3.12	Final Placement of On-board Magnetometer	53
3.13	Attitude Determination Testing with Illumination	55
3.14	Truth Rotation of CubeSat	56
4.1	Ambient Geomagnetic Vector Pre-Cage	58
4.2	Ambient Geomagnetic Vector Pre-Cage Side View	59
4.3	Magnetic Variance with Zeroed Cage Center (Vectors Scaled to $1/10^{th}$ Size - Cage Center at 0, 0, 0 mG)	63
4.4	Ambient Field vs. Zeroed Field	65
4.5	Top View of Ambient Field vs. Zeroed Field	66
4.6	Variation of B_x - Cage Center at 0, 0, 0 mG	67
4.7	Variation of B_y - Cage Center at 0, 0, 0 mG	67
4.8	Variation of B_z - Cage Center at 0, 0, 0 mG	67
4.9	Generated Magnetic Field vs. Commanded	69
4.10	Linearity of Magnetometer in Y	71
4.11	Linearity of Magnetometer in X and Z	72
4.12	X Axis Reaction Wheel Effects on Magnetometer	72
4.13	On-Board Magnetometer Offset with $B_{zi} = -1$ G	74
4.14	On-board Magnetometer Offset in 1.5 G Y_i Environment	75
4.15	Yaw about Z_b with Magnetic Field $\{0, 0, -2\}_i$ G	76
4.16	Yaw Accuracy	77
4.17	Sun Azimuth Angle	79
4.18	Optimal Method vs. TRIAD - Yaw	81

List of Tables

Table		Page
2.1	Attitude Sensor Accuracies [11]	9
3.1	Expected Magnetic Field	48
4.1	Proximity Testing	57
4.2	Measured Magnetic Field Capability of AFIT Helmholtz Cage . . .	60
4.3	Actual Magnetic Field vs. Expected Magnetic Field	61
4.4	Accuracy of OFQEA	78

CUBESAT ATTITUDE DETERMINATION AND HELMHOLTZ CAGE DESIGN

I. Introduction

1.1 *Background*

Earth orbiting satellites provide large area coverage and global access to users. Several examples of satellite products available include communications, weather data, scientific data, navigational data, and intelligence data [12, p. 14]. In rare cases, the attitude, or the orientation of the spacecraft, requires very little accuracy. More commonly, a satellite may need to point an antenna in a specific direction or an on-board imagery payload may have to point and track a specific location on Earth. As a driver in a car must determine his or her location in order to decide how to get to a final destination, a satellite must determine its current attitude in space to ascertain if it is in the desired attitude or if it must make changes to attain a desired attitude. The spacecraft subsystem that performs this determination is called the attitude determination subsystem (ADS).

In the last decade, CubeSats have become a popular method for universities and now government agencies to test attitude determination subsystems as well as other subsystems and payloads. CubeSats come in a variety of sizes ranging from 1U to 3U or 10 cm x 10 cm x 10 cm to 10 cm x 10 cm x 34 cm, respectively. These small satellites have many of the same components and subsystems as their larger brethren, but CubeSats surrender capabilities and performance in order to achieve a shorter schedule and lower cost than larger satellites. CubeSats are often used to test technologies of lower technical readiness levels (TRLs) before satellite companies or government organizations decide to invest money in furthering the technology. Meanwhile, students at the universities gain technical know-how and some experience with the design and build processes which they can utilize in their future careers in the space industry.

The CubeSat used in this research is an engineering development unit (EDU), also referred to as a “test” CubeSat, as it is not capable of operating in space primarily due to the use of non-space rated components and immature software. The EDU CubeSat does possess a communication and data handling subsystem (C&DH), power subsystem (EPS), an attitude control subsystem (ACS) which consists of reaction wheels, and an ADS as prevalent in many satellites. The ACS and ADS combine to form the attitude determination and control subsystem (ADCS). Attitude control is highly dependent upon attitude determination. The ADS of the CubeSat in this experiment relies upon Sun sensors, represented by ambient light sensors, and a 3-axis magnetometer. The combination of Sun sensors and a 3-axis magnetometer is not uncommon for satellites [13, 14].

Testing the Sun sensors requires only a light source such as a flashlight. Testing the magnetometer requires being able to modify the magnetic field in the vicinity of the magnetometer. Control of the magnetic field can be performed along one axis with a Helmholtz coil which generates a controllable magnetic field within the center of the coil when current passes through the coil. 3-axis control of a magnetic field can be achieved via a Helmholtz cage which generates a magnetic field in the same manner as the single-axis control coil; however, the cage uses three pairs of coils which are orthogonal to each other to control the magnetic field in all three axes. Helmholtz coil concepts and cages are described in detail in Chapter II.

1.2 Problem Statement

The Air Force Institute of Technology (AFIT) is progressing towards developing CubeSats for launch and operation. Based on current designs and research efforts, it is very likely that the CubeSat will have an ADCS that is dependent upon sensing the geomagnetic field in space via magnetometer and/or use the geomagnetic field to torque the spacecraft via torque coils. As a preliminary step, it is vital that AFIT begin testing attitude determination algorithms and have the ability to simulate the on-orbit geomagnetic field. Robust testing can be achieved by testing an attitude

determination algorithm on the available CubeSat and building a Helmholtz cage for testing the magnetometer and simulating the on-orbit environment. Testing the attitude determination algorithm and building the Helmholtz cage will also enable validation of future control algorithms.

The requirements are:

1. The attitude determination algorithm shall be implemented on a 3U CubeSat
2. The Helmholtz cage shall enable testing on a CubeSat as well as possible future CubeSat designs
 - (a) The cage must generate a uniform magnetic field within a volume large enough for CubeSats with deployables
 - (b) The cage must be able to simulate a dynamic on-orbit geomagnetic field
 - (c) The cage must be able to cancel the ambient magnetic field
 - (d) The cage shall generate a magnetic field large enough to provide dynamic testing of the magnetometer
 - (e) The cage shall enable possible future ADCS testing

1.3 Research Focus

The primary objectives of this research effort are to design and build a Helmholtz cage capable of generating a magnetic field of ± 2 Gauss (G) in any direction and to test an attitude determination algorithm on the test CubeSat which utilizes two individual vector measurements. The selected AD algorithm was only proven in simulation and not verified in hardware except for a brief journal article where the algorithm was combined with a Kalman filter for estimation of human body orientation [15, 16]. Secondary objectives include dynamically simulating the geomagnetic field a satellite would experience in orbit utilizing predicted geomagnetic field data from Satellite Tool Kit (STK) as well as analyzing the performance of the magnetometer and Sun sensors on-board the test CubeSat should they be used in future designs.

1.4 Methodology

The Helmholtz cage was designed by first surveying cages made by other schools and commercially available cages. The completed cage with the CubeSat on a test stand in the middle of the cage is shown in Fig. 1.1.

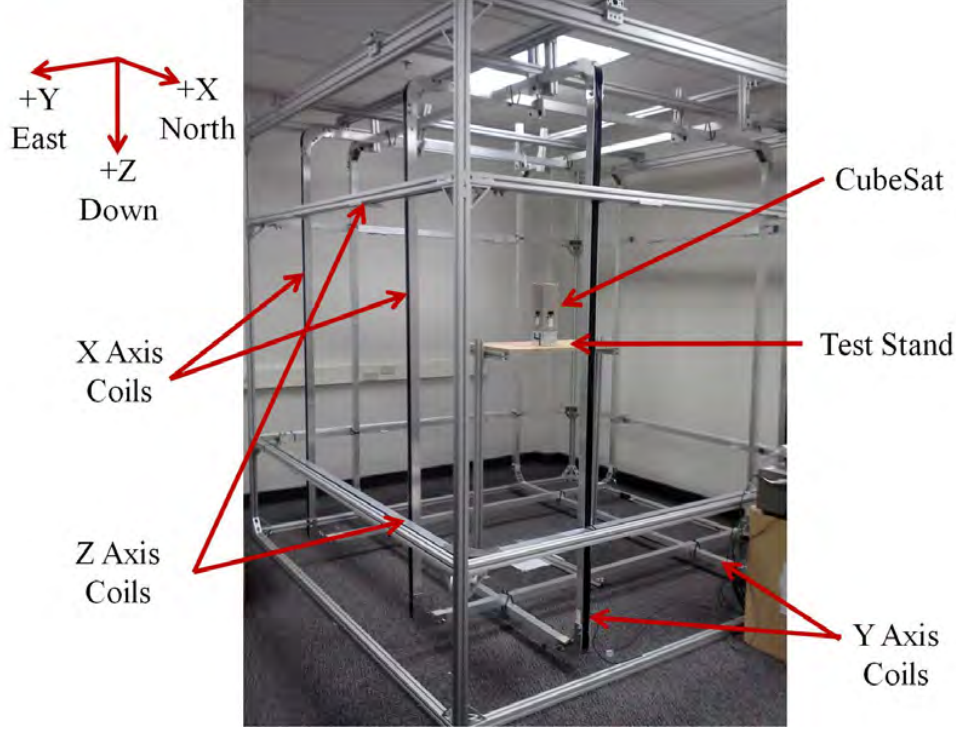


Figure 1.1: AFIT's Helmholtz Cage with Test CubeSat and Test Stand at Center

Dynamic closed-loop control of the cage is achieved entirely with MATLAB. A MATLAB script opens a STK scenario, pulls the geomagnetic field report from the scenario, checks the ambient magnetic field in the cage with the truth magnetometer, calculates the current required in each coil to obtain the geomagnetic field from the scenario, commands the coils' power supplies via the *gpib* command to the required current, and then verifies that the desired magnetic field is achieved before proceeding to the next desired magnetic field in the scenario. An attitude determination algorithm was selected by surveying suggested algorithms in text books and journal papers. The optimal fast quaternion algorithm (OFQEA) as described in [16] was selected as the algorithm has only been proven for satellite attitude determination in

simulations, and it is an optimized algorithm that can be coded onto the CubeSat with relative ease. The algorithm was implemented on the Arduino open source platform on the test model CubeSat. Attitude determination testing utilized flashlights as a light source and the Helmholtz cage to generate a controlled magnetic field in combination with the on-board Sun sensors and magnetometer. The attitude was calculated on-board the CubeSat with the results and raw data being stored on a computer for later comparisons and analysis. The test CubeSat is pictured in expanded view in Fig. 1.2.

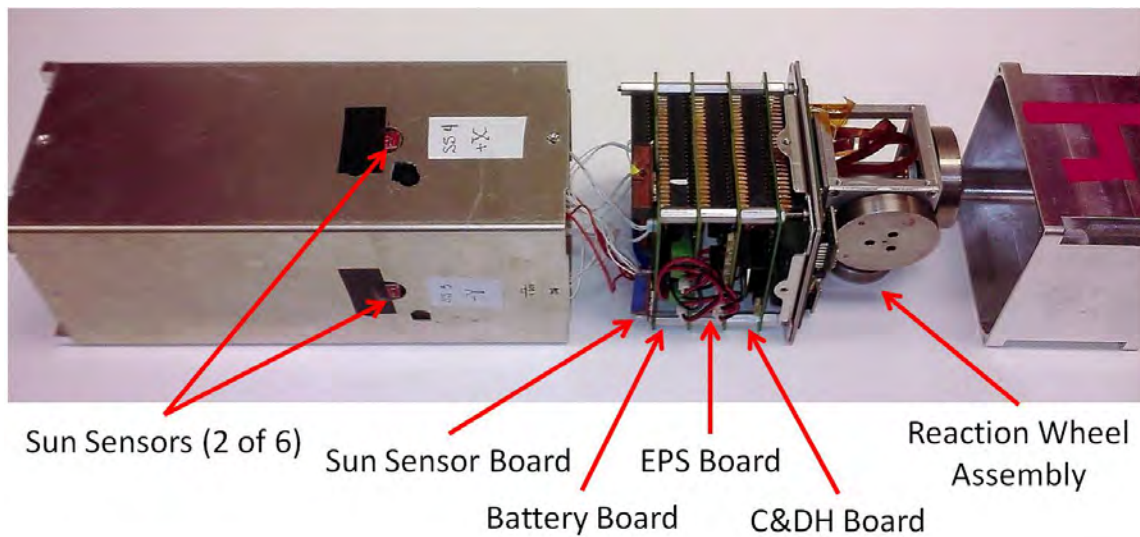


Figure 1.2: Expanded View of Test CubeSat

The expanded view of the CubeSat displays the outer casing with Sun sensors at left, the outer casing of the reaction wheel assembly at right, and the C&DH, EPS, battery board, and reaction wheel assembly in the middle.

1.5 Preview

Chapter II includes background information on the use of simulated satellites and CubeSats for technology demonstrations as well as sensors utilized for attitude determination on satellites large and small. Chapter II also discusses in depth the Earth's magnetic field including what causes the magnetic field and how the magnetic

field is affected by celestial events. Chapter II also covers the design of Helmholtz cages and coils and provides a brief synopsis of some cages that have been built to date. Finally Chapter II explores attitude determination algorithms and divides them into two categories: deterministic and optimal. Focus is on the optimal fast quaternion estimation algorithm (OFQEA) as proposed in [16] and the TRIAD method as described in [13, 14, 17, 18]. Chapter III discusses the design of the AFIT Helmholtz cage and the implementation of the selected attitude algorithm as well as the test setup for testing both the cage and the algorithm. Chapter IV presents an analysis of the ability of the cage to attain the desired ± 2 G magnetic field, the ability to zero the ambient magnetic field within the cage, and the ability to represent the geomagnetic field a satellite could experience on-orbit. Chapter IV also includes an analysis of the linearity of the on-board magnetometer, the effects of the reaction wheel on the magnetometer, and offsets associated with the selected magnetometer. Finally Chapter IV presents an analysis of the accuracy of the attitude estimation as computed via the OFQEA on-board the CubeSat versus a simulation via TRIAD using the raw data from the CubeSat attitude sensors. Chapter V provides final conclusions as well as recommendations for future work.

II. Background

This chapter will discuss CubeSats, different sensors used for attitude determination, the utilization of Helmholtz cages to simulate the geomagnetic field in the space environment, and several different attitude determination algorithms. This chapter also provides the theory and knowledge that was incorporated into the design of the cage and the implementation of the attitude determination algorithm in this research.

2.1 *Simulated Satellites*

The test CubeSat utilized in this research effort is an example of a simulated satellite. Simulated satellites provide the opportunity for researchers and satellite developers to test satellite hardware and software on the ground where issues can be easily resolved and subsystems can be more easily analyzed, rather than launching an untested satellite and hoping that Murphy's Laws can be evaded. The CubeSat described in this chapter and used in this experiment is even more simplified than some simulated satellites because the majority of parts are not space-rated. However, it has many of the subsystems that most satellites require including the Electrical and Power Subsystem (EPS), attitude determination and control subsystem (ADCS), telemetry, tracking and command (TT&C), command and data handling (C&DH), and structures [12]. The CubeSat is approximately 10 cm x 10 cm x 34 cm or 3U.

Many CubeSats have been built and launched like QuakeSat from Stanford which tested earthquake precursor sensing [19] and GeneSat-1 from NASA and Santa Clara University which housed a micro-laboratory [20]. Delfi-C³ from the Delft University of Technology is another example of a 3U CubeSat. Control for Delfi-C³ is composed of hysteresis rods which were tested via a Helmholtz cage similar to the one described in this research [9]. The University of Michigan (U-M) also had a 3U CubeSat called the Radio Aurora Explorer (RAX) which studied the formation of magnetic field-aligned plasma irregularities in the lower polar ionosphere. The students at U-M also built a Helmholtz cage to calibrate the magnetometers and simulate the on-orbit

geomagnetic environment [10]. Both the U-M and TU Delft cages will be discussed in further detail in this chapter.

The CubeSat for this experiment was designed and tested in a traditional university 10 week quarter and then built in the following 10 week quarter in 2011 without the intent of launch but rather to gain experience. The course is designed to give students an understanding of each of the subsystems and how they integrate with each other. The course also provides the opportunity to learn about common problems that spacecraft face like surviving launch and the harsh environment of space as well as meeting constraints of cost, schedule, and performance. The end result of the program is that the individuals who were in the course will be able to make informed decisions in their future work managing space programs for the United States Air Force. Before designing a CubeSat, students at any university have to determine what sensors they wish to incorporate into the design. Available sensors are described in the next section.

2.2 *Attitude Sensors*

This section will present attitude determination sensors utilized today for attitude determination, but first it's important to understand the need for multiple sensors. The basic representation of a satellite is a rigid body with 3 rotational degrees of freedom (DOF) about a body frame $\{\hat{\mathbf{b}}\}$. The body frame $\{\hat{\mathbf{b}}\}$ rotates and translates with the satellite as compared to the inertial frame $\{\hat{\mathbf{i}}\}$ which is a non-rotating frame. The inertial frame is an important frame of reference if the attitude of the spacecraft is to be related to any other element in 3-D space. These reference frames are depicted in Fig. 2.1.

Limited attitude knowledge can be estimated if the satellite only has one sensor. Imagine a satellite has a Sun sensor with the purpose of detecting the Sun and its line of sight is along the \hat{b}_3 axis of the satellite as shown in Fig. 2.1. If the CubeSat is oriented with respect to the Sun with the body frame Sun vector \hat{s}_b colinear with

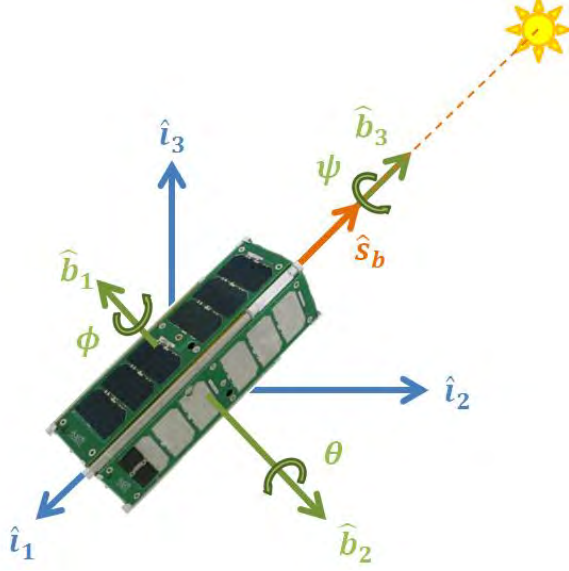


Figure 2.1: CubeSat Reference Frame Unit Vectors with Sun

\hat{b}_3 as shown in Fig. 2.1, then the angle ψ cannot be determined. If the Sun was completely out of view none of the angles (ψ , ϕ , or θ) could be determined. By adding another type of sensor and by selecting the proper combination of sensors, full attitude determination capability is possible [11] [12, p. 375]. Different sensors vary in levels of accuracy and cost. Possible sensors will be discussed next.

Options for attitude sensors in satellites include Earth sensors, Sun sensors, star sensors, gyroscopes, and magnetometers [21]. As an overview, the attitude determination accuracy of each of these sensors is listed in Table 2.1.

Table 2.1: Attitude Sensor Accuracies [11]

Sensor	Accuracy
Earth Horizon	0.05° GEO 0.1° LEO
Sun	0.01°
Star	0.0005°
Gyroscope	0.001°/hr
Magnetometer	N/A

All of the sensors in Table 2.1 will be described in detail in the rest of this section, but note that the Attitude Determination Subsystem (ADS) on the test model CubeSat relies solely upon six Sun sensors and a 3-axis magnetometer.

Earth horizon sensors can sense the radiance of the horizon providing attitude determination accuracy of 0.05° at a geostationary orbit (GEO) or 0.1° at a low Earth orbit (LEO) [11]. The horizon sensors typically consist of four components: a scanning mechanism, an optical system, a radiance detector, and signal processing electronics. If the spacecraft is a spinning spacecraft, the scanning mechanism is the spinning of the satellite. For non-spinning spacecraft, a momentum wheel may be utilized specifically for the Sun sensor to provide the scanning ability or perhaps a slowly rotating turret within the sensor assembly. The optical system includes a filter to limit the incoming light and a lens to focus the image on the radiance detector. The radiance detector is tuned to the desired spectral radiance of the Earth and as such will then detect, or not detect, the presence of the Earth. This data is then compared with respect to a reference time and translated into acquisition of signal (AOS) or loss of signal (LOS) based on whether the output from the detector is increasing against some threshold or decreasing against some threshold respectively. The reference times since AOS or LOS combined with the scan rate, or in the spinning satellite case the spin rate, allows for the calculation of the angle with respect to Earth's horizon from the time data [14].

Sun sensors are the most commonly utilized sensor [14, 21]. Sun sensors utilize photocells to detect sunlight and can be divided into three groups: analog sensors, Sun presence sensors, and digital sensors. In an analog sensor, the angle of the Sun with respect to the normal vector of the sensor is calculated as a function of the output current of the photocell(s). The output current is calculated by

$$I(\theta) = I(0)\cos(\theta) \quad (2.1)$$

where θ is the angle between the Sun vector and the normal vector of the Sun sensor, $I(\theta)$ is the current as a function of θ , and $I(0)$ is the current when the angle of incidence is zero [14]. As opposed to analog Sun sensors, Sun presence sensors provide a constant current whenever the Sun is in the very narrow FOV of the sensor. Sun

presence sensors are used for safeguarding instrumentation, like light sensitive star trackers, and activating hardware [14]. Finally, digital sensors utilize a narrow slit to minimize their FOV in combination with a variety of photocells that output a digital signal which can be exploited to determine the angle of the Sun with respect to the null or centerline of the slit [14]. Sun sensors can be used to estimate the angle of the Sun with respect to the spacecraft to within 0.01° [11], and for most applications, the Sun can be approximated as a point source [14].

Star sensors compare stored maps of stars with collected star data to calculate a satellite's attitude [21]. Star sensors consist typically of a Sun shade, an optical system, an image definition system, a detector, and an electronics assembly. The Sun shade keeps ambient light from affecting the sensitive sensors. The optical system projects an image of the visible stars onto the focal plane from which the image definition system selects which portion to make visible to the detector. From here, the detector turns the remaining image into an electrical signal which is then multiplied and filtered by the electronics assembly [14]. Star sensors can be accurate to 0.0005° [11]. They are typically costly and bulky and they require more power than other sensor options [11, 14].

Standard gyroscopes use a spinning mass, similar to a top, to measure changes in attitude. As the mass is rotated perpendicular to the spin vector the mass will precess meaning the rotation axis changes direction. The precession angle and rate can be used to compute the change in attitude [21] with some gyroscopes being able to provide $0.001^\circ/\text{hr}$ drift accuracy [11]. The CubeSat in this research effort utilizes the ITG-3200 gyroscope sensor package on the SEN-10183 9-DOF sensor stick from Sparkfun. This package consists of three independent vibratory microelectromechanical (MEMS) gyroscopes, one for each of the three axes. Vibratory MEMS gyroscopes work on the principle that as a mass oscillating at a mode is rotated about a body fixed axis the resulting Coriolis acceleration causes the mass to move in a different mode. The deviance is captured by sensors in the gyro and is related to an angular rate [22, 23]. Ring-laser gyroscopes are another form of gyroscope that use lights and mirrors. As

the spacecraft rotates the received frequency of the laser changes with the change in distance that the beam must travel. The change in frequency is then related to a rotation rate [21].

Magnetometers are vector sensors that detect the orientation and magnitude of Earth's magnetic field, described in Section 2.3, for attitude determination. The two main categories of magnetic field sensors are induction magnetometers and quantum magnetometers [14]. Induction magnetometers can further be divided into either search-coil or fluxgate magnetometers. A search-coil magnetometer consists of a solenoid coil wrapped around a ferromagnetic core. When the coil is subjected to a magnetic field an electromotive force (EMF) is induced in the coil resulting in a voltage in the coil. However, the coil is affected only by magnetic flux along the axis about which the coil rotates. A fluxgate magnetometer consists of a primary solenoid coil, core, and secondary solenoid coil. The primary coil has an alternating current yielding a variation in the core magnetic field value which is also affected by the surrounding magnetic field. The secondary coil experiences an induced EMF as the core magnetic flux density fluctuates. This EMF is compared with the original applied current to calculate the surrounding magnetic field intensity [14].

The other category of magnetometer is the quantum magnetometer which utilizes atomic properties to measure magnetic field magnitude and direction. An example is the proton precession magnetometer where a hydrogenous sample is placed in a strong magnetic field and once the strong field is removed, the sample retains a residual smaller magnetic field. The smaller field will precess when influenced by an external field. The precession is measured yielding a measurement of the external magnetic field. However, this does not provide direction information. Another type of quantum magnetic sensor utilizes optical pumping. In optical pumping, a light source produces a beam of collimated, or one direction, resonance radiation which passes through vapor. The ambient magnetic field is then measured as a function of the vapor transparency [14].

The CubeSat utilized in this research effort is equipped with a HMC5843 3-Axis Digital Compass IC from Honeywell on-board a SEN-10183 9 degrees of freedom (DOF) board available from Sparkfun. This package consists of three independent vibratory microelectromechanical (MEMS) gyroscopes, one for each of the three axes. The MEMS gyroscope provides a small gyroscope package that required minimal space with dimensions of $4 \times 4 \times 0.9 \text{ mm}^3$ [22]. The magnetometer can sense the geomagnetic field vector in 3-dimensions via Honeywell’s Anisotropic Magnetoresistive (AMR) technology [24]. AMR technology utilizes a Permalloy or nickel-iron alloy thin film on a silicon wafer. The Permalloy is patterned in a resistive strip. As the strip is introduced to a magnetic field the resistance of the strip changes. The combination of four of the resistors with a Wheatstone bridge allows for the measurement of the magnitude and direction of the magnetic field [25].

Magnetometers are more useful in LEO than GEO, due to the more consistent and stronger geomagnetic field as described in Sec. 2.3. The next section covers the geomagnetic field which is the magnetic field that a satellite magnetometer senses for attitude estimation.

2.3 Geomagnetic Field

The geomagnetic field, or magnetic field of the Earth, can be approximately represented as a magnetized iron bar tilted approximately 11° from the Earth’s spin axis [1] as shown in Fig. 2.2.

The primary component of the geomagnetic field is the dipole field with fields ranging from 0.3 to 0.6 Gauss (G) at the geomagnetic equator and pole, respectively [1, 26]. The center of Earth consists of a solid iron ball, also known as the inner core. The core spins at a separate rate faster than that of the Earth and is housed in a layer of liquid iron called the outer core which is a dynamic, electrically conducting fluid [26] as shown in Fig. 2.3.

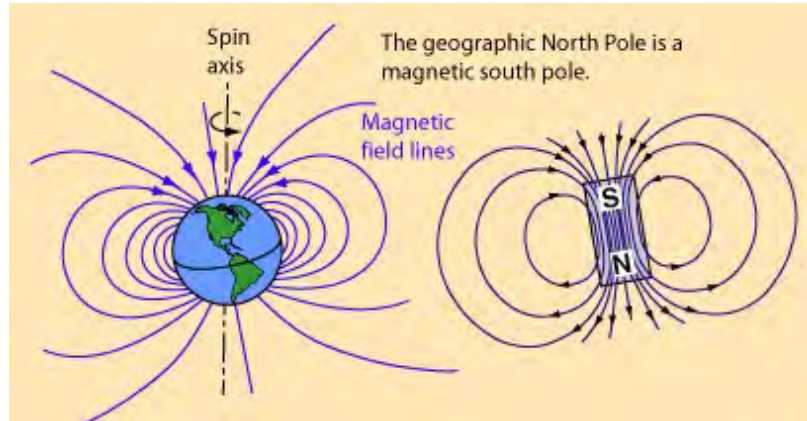


Figure 2.2: Representation of Earth's Magnetic Field [1]

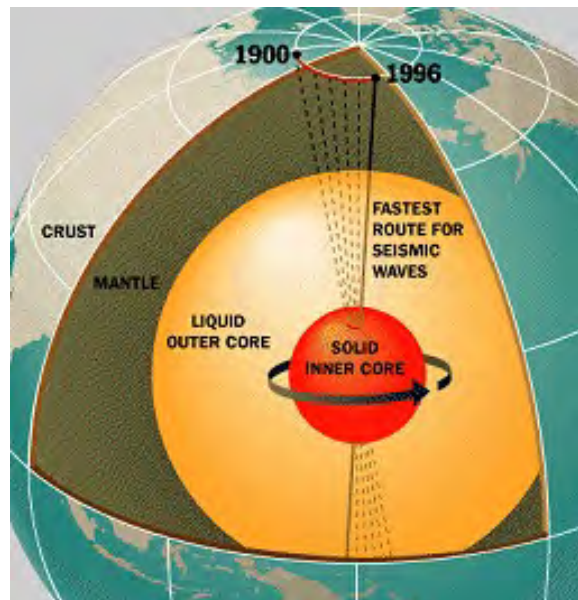


Figure 2.3: Earth's Core [2]

The outer core produces the Earth's magnetic field through the dynamo effect [2]. In the dynamo effect, heat from the inner core causes convection in the outer core fluid as it cools towards the Earth's surface. This convection of the outer core along with forces from Earth's rotation causes shearing in the outer core generating magnetic fields [27]. The magnetic field is constantly changing in magnitude and direction. The North Pole in the 20th century moved North at an average speed of 10 km per year and also weakened by 10% [26]. The geomagnetic field also completely

changes direction approximately every 200,000 years, but these reversals are randomly distributed. Such a reversal takes several thousand years to complete [27].

The second component of the geomagnetic field comes from magnetized rocks in the Earth's outermost shell, called the lithosphere. These rocks contribute to the geomagnetic field at the Earth's surface a few hundred nanoTesla (1 nT equals 0.01 mG). The final component comes from the ionosphere and magnetosphere [26] which will be described in Section 2.3.1.

If a magnetic field was in free space without any surrounding materials, the magnetic flux would be equivalent to

$$\vec{B} = \mu_o \vec{H} \quad (2.2)$$

where \vec{B} is the magnetic flux with units of Newtons per Amp meter, μ_o is the permeability of a vacuum in units of Newtons squared per Amperes squared and \vec{H} is the magnetic field strength in Amperes per meter [26].

However, Eqn. 2.2 represents a perfect case. Materials within the environment of a magnetic field affect the magnetic field vector. The response of a material to external magnetic fields can be classified as paramagnetic, diamagnetic, or ferromagnetic. A paramagnetic material produces magnetization in the same direction and proportional to the applied field [26, 28, 29]. A diamagnetic material produces magnetization in the opposite direction of the magnetic field. Diamagnetism is a property of all materials and is a very weak effect [29]. Paramagnetism has a stronger effect than diamagnetism, but the greatest effect comes from ferromagnetism. In ferromagnetism, magnetic moments within the material become aligned with each other when influenced by a magnetic field and remain aligned when the field is not applied [28]. Ferromagnetism can produce magnetizations several orders of magnitude greater than the applied field [26, 29]. Iron, cobalt, and nickel are examples ferromagnetic materials [28]. The term ferromagnetism is used as ferrum, which is Latin for iron, is the most common and noticeable example [29].

2.3.1 Magnetosphere and Ionosphere. As previously mentioned, the geomagnetic field is affected by the magnetosphere and ionosphere and more specifically from the current flow of ions and electrons in these areas. As high-velocity plasma, or solar wind, from the Sun reaches the Earth it compresses the geomagnetic field on the Sun facing side of the Earth and extends the field on the opposite side. The region shaped by this phenomenon is called the magnetosphere. Within the magnetosphere the motion of charged particles is dominated by the geomagnetic field [26].

The ionosphere forms the inner edge of the magnetosphere. The ionosphere exists at roughly 50 to 1000 km above the Earth. At these altitudes, the atmospheric density is low enough for free electrons to exist for short periods of time [26]. Gas atoms absorb solar radiation resulting in a free electron and a positively charged ion [30]. The higher the solar radiation, the higher the number of ions [26]. The time of day and solar activity therefore has an effect on ionization.

Solar wind shapes the magnetosphere by compressing the sunward side of and extending the magnetosphere on the other side of the Earth as shown in Fig. 2.4. The ionosphere is well within the magnetosphere which is also shown in the figure. It's important to note that the figure is not drawn to scale, but it shows the general region that specific models represent as well as the compression of the magnetosphere [3].

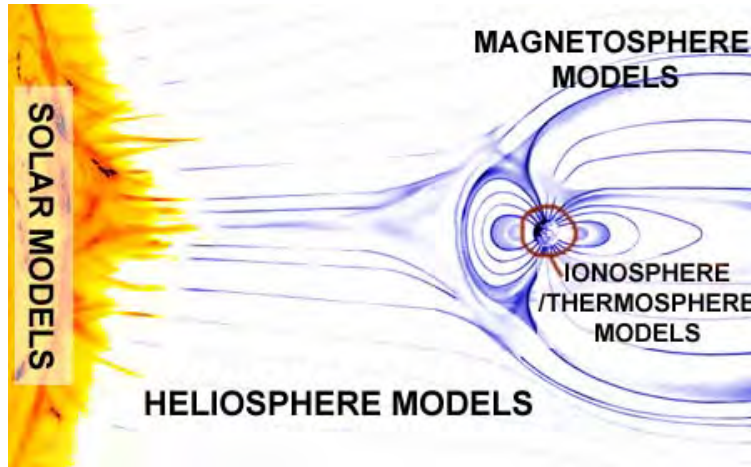


Figure 2.4: Earth's Ionosphere and Magnetosphere - (not drawn to scale) [3]

2.3.1.1 Diurnal Fluctuations. The geomagnetic field experiences minor fluctuations occurring in a 24 hour cycle. Ionization of the ionosphere occurs as ultra-violet rays and X-rays from the Sun reach the ionosphere causing an increase in the conductivity of the ionosphere. The ionization is most intense at midday with the particles recombining after dusk. The Sun also heats the ionosphere creating thermotidal winds which combine with tidal winds caused by the gravitational pull of the Sun and the Moon to create the “ionospheric dynamo”. The conductive ionosphere passes through the geomagnetic field generating a current which flows in a counterclockwise vortex in the northern hemisphere and a clockwise vortex in southern hemisphere. This current flow causes minor diurnal fluctuations in the geomagnetic field [31]. The amount of solar radiation varies with the solar cycle, altitude, latitude, time of day, and season which in turn affects the ionospheric dynamo [4,31]. The diurnal increase in the geomagnetic field is evident in Fig. 2.5.

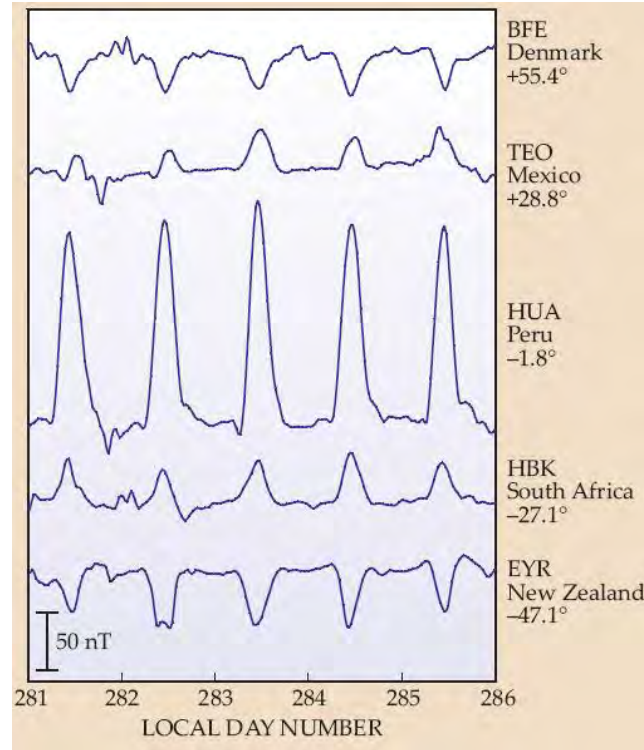


Figure 2.5: Diurnal Variations at Select Observatories [4]

Fig. 2.5 presents the horizontal intensity, or the square root of the sum of the squared Northern vector and squared Eastern vector of the geomagnetic field, for several geomagnetic field observatories ranging from low Southern to high Northern latitudes. Locations near the equator experience the largest diurnal fluctuation as they experience both the northern and southern hemisphere vortexes. Locations near the poles experience reversals in polarity [4]. AFIT is located at approximately 40° North and should experience diurnal variations less than 50 nT (0.5 mG) which is well below the average horizontal geomagnetic field across the surface of the Earth of 500 mG [8].

A far greater impact on the geomagnetic field occurs from magnetic storms in the magnetosphere. Coronal mass ejections or high-velocity plasma from the Sun can cause a buildup of energy in the magnetosphere forcing the magnetospheric electric circuit to pass through the ionosphere. One of the largest magnetic storms occurred in October 2003. Observatories at high latitudes experienced geomagnetic field variations up to 3,000 nT (30 mG). These storms are more prevalent during times of sunspot maxima coinciding with the 11 year solar cycle [4].

2.3.2 Geomagnetic Models. At least 90% of the Earth’s measured magnetic field is due to the dynamo effect of the Earth’s core. The measured field for both the surface of the Earth and in orbit has been modeled by the National Oceanic and Atmospheric Administration (NOAA) in their International Geomagnetic Reference Field (IGRF) model and by the National Geospatial-Intelligence Agency in cooperation with the United Kingdom’s Defense Geographic Center in their World Magnetic Model (WMM). These models do not take into account the remaining 10% [32] that is due to the ionospheric diurnal fluctuations and magnetospheric storms [4].

The Satellite Tool Kit (STK), offered by Analytical Graphics Incorporated (AGI), is a software package which is commonly used for modeling and simulating a variety of platforms including satellite, UAV, and missile. One of the available tool-kits for STK is the Space Environment and Effects Tool (SEET). SEET can

provide an analysis of geomagnetic fields which a spacecraft would experience at any given point in orbit or throughout the satellite's lifetime. This analysis can be based upon IGRF data (i.e. not accounting for magnetosphere and ionosphere effects), but there is the option to include local-time-dependent data from the Olson and Pfitzer Tilt Dependent Model from 1977 [33]. The Olson-Pfitzer model takes into account currents from the magnetosphere [34, 35]. Dynamic control of the AFIT Helmholtz cage utilizes both IGRF data and the Olson-Pfitzer model in the SEET analysis of the geomagnetic field a satellite would experience on-orbit. Chapter III discusses the interface between the cage and SEET analysis required to provide dynamic cage control.

2.4 *Helmholtz Coils*

A magnetic field can be generated for testing the ADS of a satellite as well as to simulate the geomagnetic fields that a satellite would experience during an orbit or throughout its lifetime as discussed in the previous section. One device capable of generating a uniform magnetic field is the Helmholtz coil. The Helmholtz coil is named after Hermann von Helmholtz (1821-1894), a German scientist and philosopher known for his contributions to electrodynamics, mathematics, and meteorology among many other sciences. As shown in Fig. 2.6, a Helmholtz coil consists of a pair of coils parallel to each other where each coil consists of a number N wrappings. A magnetic field B results when charge is in motion, i.e. as current I passes through the coil pair following the right-hand rule.

The magnetic field at the mid-point between the two coils is calculated via

$$B = \frac{32\pi NI}{5\sqrt{5}a} \times 10^{-7} \quad (2.3)$$

where B has units of Tesla, a is the radius of the coils, N is the number of turns per coil, and I is the current passing through the coils [5]. Separating the coils by

Helmholtz Coils

B = magnetic field (tesla)
 I = current (amperes)

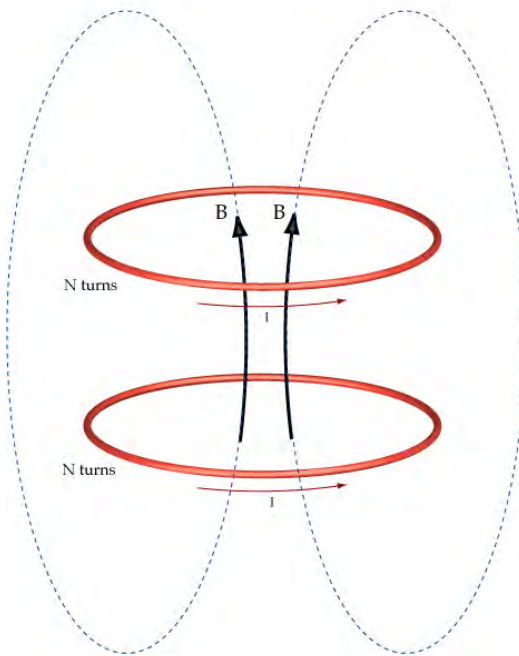


Figure 2.6: Helmholtz Coil Pair [5]

a distance equal to the radius of the circular coils provides a uniform magnetic field across in the mid-plane of the coil, as shown in Fig. 2.7.

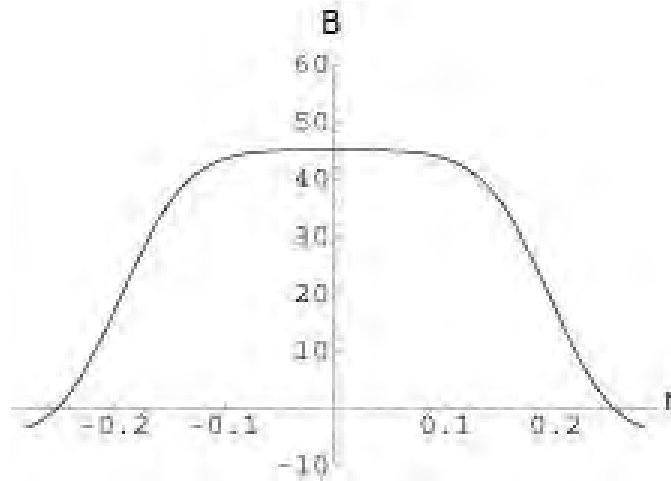


Figure 2.7: Uniform Field for Circular Coils [5]

The field for coils with a radius of 0.2 meters is uniform to approximately 0.1 meters from the centerline with a total length of 0.2 meters of homogeneity as shown in Fig. 2.7 [5]. The magnitude of the magnetic field B will vary with the applied current. Changing the distance between the coils changes the uniformity of the field as shown in Fig. 2.8.

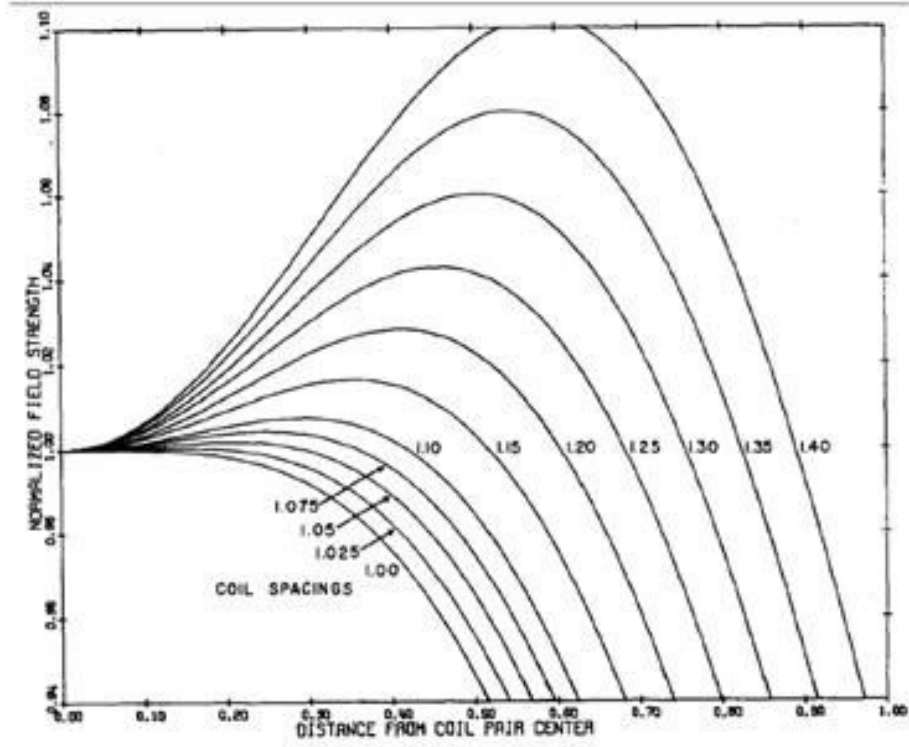


Figure 2.8: Magnetic Field Uniformity for a Circular Coil [6]

As the spacing between coils increases, the magnetic field starts to vary and grow then dissipate with increased distance from the centerline. Having a homogeneous field, as occurs when the spacing of the coils is equal to the radius of the coils, provides a homogeneous test area. Larger diameter coils provide a larger homogeneous field.

Square coils can be utilized instead of circular coils in the design as they provide a wider uniform field parallel to the coils as compared to circular coils [36]. The governing equation for the magnetic field B at the center point of a square coil pair

is

$$B = \frac{2\mu_o NI}{\pi a} \frac{2}{(1 + \gamma^2)\sqrt{2 + \gamma^2}} \quad (2.4)$$

where μ_o is the permeability of a vacuum, $4.95\text{e-}5$ Tesla-in/Amp, N is the number of wrappings, I is the current passing through the coils, a is half the length of a side of the coil, and γ is the ratio of the distance between the two coils $2b$ and the length of the side of a coil $2a$ shown in Fig. 2.9.

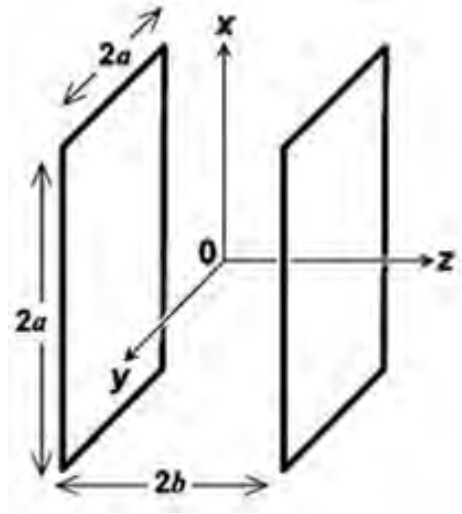


Figure 2.9: Square Helmholtz Coil Pair ©IEEE [7]

In order to achieve a homogeneous field at the mid-point of the square Helmholtz coil pair γ is 0.5445 and therefore the spacing between coils is 0.5445 times the length of a coil [7]. If the coils are not properly spaced, a profile similar to that of Fig. 2.8 is achieved. Actual coils have rounded corners as a function of the wire's flexibility resulting in some error in Eq. (2.4).

2.5 Helmholtz Cages

The European Space Agency (ESA) utilizes 2 pairs of square Helmholtz coils in testing and measuring the magnetic properties of equipment and spacecraft components [37]. Utilizing three orthogonal pairs of Helmholtz coils permits 3-axis control of a magnetic field within the coils. This configuration of three orthogonal square

coil pairs is often referred to as a “Helmholtz cage”. Commercial cages are available from the Macintyre Electronic Design Associates (MEDA), Inc [8]. Several universities have built Helmholtz cages to develop and test the ADCS for CubeSats and to simulate the geomagnetic space environment, as defined in Sec. 2.3. The Naval Post Graduate School (NPS) in Monterey, CA, the University of Michigan (U-M) in Ann Arbor, MI [10], and the Delft University of Technology in the Netherlands [9,38] all have Helmholtz cages built by students in cooperation with their professors. The university cages are much less expensive than the commercial cage and they provide a learning opportunity for the students. The MEDA Inc., U-M, and TU Delft cages will be discussed in further detail in the rest of this section beginning with the commercial cage offered by MEDA, Inc.

2.5.1 MEDA, Inc. Helmholtz Cage. The MEDA Corporation offers 1, 2, and 4 meter systems. The information provided in the rest of this section comes from the specification sheet for the 2 m cage [8]. The 2 m standard Helmholtz cage includes three square Helmholtz coil pairs with approximately 2 m sides for generating and controlling the magnetic field, an additional three square concentric coil pairs for controlling gradients, 6 power supplies with one power supply (PS) per coil pair, a control magnetometer, and the ability to control the cage by personal computer (PC). A fluxgate sensor, which is part of the magnetometer, along with the field control electronics and power supplies compensate for ambient magnetic fields from surrounding electronics near the center of the cage. A PC with software designed specifically for the cage is used to control the polarity and magnitude of the magnetic fields as well as the gradients. A single power distribution unit is used to turn the entire cage including the power supplies, magnetometer, and PC on or off. The cage comes in a kit with a packaged coil assembly, rack assembly, and PC [8]. The cage does not require an external support structure as the university cages do as discussed later in this chapter. Instead, the support for the coils provides the structure for the cage. The assembled 2 meter 3-axis coil system is shown in Fig. 2.10.



Figure 2.10: MEDA Helmholtz Cage [8]

MEDA's 2 meter coil system is capable of generating controlled fields up to ± 1 G (100,000 nT) and has field uniformity within 0.03% of the applied field in a 20 cm (approximately 8") diameter sphere at the center of the coil system. The middle size coils are to be oriented North representing the X-axis control and the smallest coils point East representing Y-axis control. Some design recommendations for the cage include the ambient temperature range between 22 and 24°C, raising the cage ten inches above reinforced concrete flooring, ensuring ferromagnetic objects are at least 15 feet from the edge of the coils, and the coils be at least 50 feet from parking lots, roadways, and railroad right-of-ways. The concern when placing the cage is that the cage can compensate for uniform changes, i.e. consistent changes across the entire control volume, but not for gradient changes [8].

2.5.2 Delft University of Technology Helmholtz Cage. Delft University of Technology (TU Delft) in the Netherlands built a Helmholtz cage as part of the design process for their Delfi-C³ CubeSat which launched in 28 April 2008. Delfi-C³ tested Thin Film Solar Cells from DutchSpace and a digital Autonomous Wireless

Sun Sensors from TNO, the Dutch institute for science. Gradual rotation, 0.2 to 10 degrees per second, of the CubeSat was desirable for both payloads and so TU Delft utilized a Passive Magnetic Attitude Control System (PMAS). PMAS includes a permanent magnet designed to align the CubeSat with the geomagnetic field as well as two hysteresis rods for damping excessive angular velocity [38].

One of the design requirements for the Helmholtz cage included that Delfi-C³ must fit inside the cage with antennas deployed. The minimum length of the cage was therefore 1 meter and the minimum volume was 1 m³. With the Helmholtz spacing requirement of 0.5445, the coils needed to be approximately 2 m x 2 m. The final design includes coils with outer dimensions of 2.05, 1.95, and 1.85 meters. The parallel coils can be moved further apart to permit a larger test volume with the consequence of losing the homogeneous field as discussed in Sec. 2.4. Representations of the standard spacing and expanded coils are provided in Fig. 2.11.

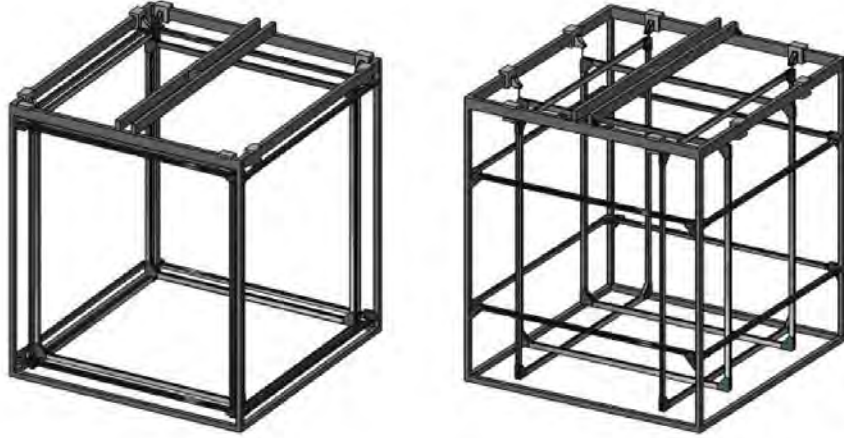


Figure 2.11: Delft University of Technology Cages [9]

The cage at TU Delft was built during the latter half of 2006. The cage is powered by 6 power supplies capable of generating up to 30 V and 10 A which are controlled by LabView software. Each coil in the cage has 83 windings. A webcam is used to record the rotation of a test object and then the video files are analyzed later to determine the angular rotation rate [38]. TU Delft used an AlphaLab DC MilliGauss Meter which is a 3-axis magnetometer for measuring the flux density at

one location. This magnetometer consists of three magnetoresistive sensors and can measure ranges of ± 1999.9 and ± 199.99 mG providing either a larger magnitude or a higher resolution measurement, respectively. There is a digital display as well as three separate BNC outputs for a PC connection [39]. This magnetometer will be discussed further in Chapter III as it is part of AFIT’s Helmholtz cage as well.

TU Delft’s cage is capable of producing any field between 0 and 7.5G with a variation of the coil spacing. The reinforced concrete in the lab area causes the field to vary as much as 30 mG within the cage [38].

2.5.3 University of Michigan Helmholtz Cage. The University of Michigan (U-M) built a Helmholtz cage as part of their Radio Aurora Explorer (RAX) CubeSat project. RAX-1 launched in November 2010 and completed its mission in May of 2011 due to power issues. RAX-2 was launched in October 2011 and is currently studying the formation of magnetic field-aligned plasma irregularities in the lower polar ionosphere. Knowledge of the spacecraft’s attitude, and more importantly the direction that the spacecraft antenna are pointed, is important to accomplishing their science objectives. A magnetometer aids in determining the attitude of RAX while RAX is also passively magnetically stabilized to align along an axis with the geomagnetic field. Position data from GPS and TLEs is used with the IGRF database to obtain geomagnetic data which is then compared to data from the magnetometer to determine the CubeSat’s orientation. A Helmholtz cage was designed and built by the U-M students to characterize and calibrate the magnetometer within a working spacecraft. A picture of U-M’s Helmholtz cage depicting the cage, workstation, and variable resistor is provided in Fig. 2.12.

U-M utilized much of the design information from Delft University and built upon it by adding an interface with STK. Requirements for the Helmholtz cage include [10]:

- Be capable of generating a magnetic field of approximately 2 G



Figure 2.12: University of Michigan's Helmholtz Cage [10]

- Large enough to fit a 3U CubeSat with a deployable antenna
- Be easily disassembled and stored

The outer support for the coils consists of aluminum T-slot framing and is 2 m x 2 m x 2 m. The 24 AWG wire was wrapped around aluminum U-channel and the entire structure was mounted on caster wheels. Each coil consists of 4 parallel wires wrapped 90 times totaling 360 loops per coil. Approximately 60,000 feet of wire was used to wrap all 6 coils. A variable resistor is used to ensure that the current draw would be equivalent across the 4 parallel wires in a loop. Three DC power supplies are used with one PS for each pair of coils [10]. The power supplies include a HP 6643A capable of 0-35 V and 0-6 A up to 200 W; a HP 6653A capable of 0-35 V and 0-15 A up to 500 W; a HP 6632A capable of 0-20 V and 0-5 A up to 100 W [40]. The power supplies are controlled by a PC via GPIB/HPIB cables to a GPIB/USB adapter. Generated field strengths are $([-0.2 \text{ G}, 0.6 \text{ G}], [0 \text{ G}, 0.35 \text{ G}], [-.5 \text{ G}, 0.6 \text{ G}])$ in the X, Y, and Z directions respectively which falls short of the requirement of 2 G. The students utilized what was on hand, specifically the 24 AWG telephone wire

and power supplies, and they suggest improving the system with upgraded power supplies [10].

The power supplies are controlled via MATLAB's Instrumentation Toolbox. The *gpib* function in MATLAB is used for commanding the PS and to get feedback of the generated field from a Honeywell HMR2300 magnetometer [10] providing closed loop control. The HMR2300 has a magnetic field range of ± 2 G with a resolution of 0.067 mG [41]. STK *Connect* provided an interface between MATLAB and STK so that real-time position and attitude data were read at a 1 second time step from a running STK simulation. This data was then fed into a MATLAB function that could calculate the 3-axis magnetic field from the IGRF model.

An automatic calibration function is written in a MATLAB file which commands each PS individually to vary the voltage within acceptable limits. If only one coil pair is energized and changes are seen in the other two axes the function estimates how the other coils should be energized to remove the error. Calibration and characterization of the cage is recommended before every experiment and requires 2-3 minutes. Another calibration technique includes mapping the magnetic field within the control volume. A wood board was laid horizontally across the mid-section of the cage and marked for 11 data points along the x-axis and 39 points along the y-axis. The HMR2300 magnetometer is then placed at each grid point and the magnetic field strength is recorded and mapped. The strength of external magnetic fields and noise can be measured within the cage. Calibrating the cage yielded the ability to update the code if the feedback sensor is moved.

The students recommend future work including fully mapping the field in the cage with a three-dimensional grid, upgrading power supplies, and being able to create positive and negative fields. They also plan to include lights for Sun sensors and a rate table for gyro characterization [10]. A further application of the cage, beyond simulating the space environment and calibrating the magnetometer, included characterizing the residual dipole of the RAX CubeSats [42].

2.6 Attitude Determination

Now that attitude sensors, the geomagnetic field, and Helmholtz coils and cages have been discussed they can be incorporated into the discussion of attitude determination. A satellite's attitude can be represented in several ways including Euler angles, Rodriguez parameters, eigenaxis rotations, and quaternions. These representations as well as the kinematic equations of motion are described in almost any literature describing attitude determination including [13,14,43,44], and the 'Survey of Attitude Representations' [45] which may be the most inclusive literature on the subject. As one of these books or articles is likely available to the reader the representations will not be discussed in depth in this research effort. The focus of this research will be more on how the attitude is estimated.

Methods of three-axis attitude determination are typically divided into two groups: deterministic and optimal [13] or as described in [18] deterministic and statistical. The deterministic method utilizes two unique vectors to determine a satellite's attitude as described in Sec. 2.6.1 and the optimal/statistical method, from here on referred to as the optimal method, is based upon minimizing Wahba's loss function as described in Sec. 2.6.2.

2.6.1 Deterministic Attitude Determination. A deterministic method of attitude determination utilizes two independent vectors, i.e. data from two sensors, to estimate a satellite's attitude. The TRIAD algorithm is commonly referenced in literature as the method of deterministic attitude determination [13, 14, 17, 18]; however, it may also be entitled the algebraic method [14] or as the *triad* algorithm [13, 18]. In 1981 Schuster coined the term TRIAD based upon an IBM Federal Systems, Inc. document entitled "Tri-Axial Attitude Determination System" however Schuster credits the algorithm to a paper by Black in the AIAA Journal in 1964 [17].

The TRIAD algorithm utilizes a minimal set of data to determine the spacecraft's attitude via the direction cosine matrix describing the rotation from the inertial to body reference frame. TRIAD utilizes two unit vector measurements in the space-

craft body frame [13,18] and is described in [13] as being “naive but excellent”. As a commonly used example [16], a Sun sensor and a magnetometer will provide data in the body frames \vec{S}_b and \vec{M}_b , and \vec{S}_i and \vec{M}_i will represent the inertial Sun and magnetic vectors, respectively. The magnetic and Sun vectors in the inertial and body frame are depicted in Fig. 2.13.

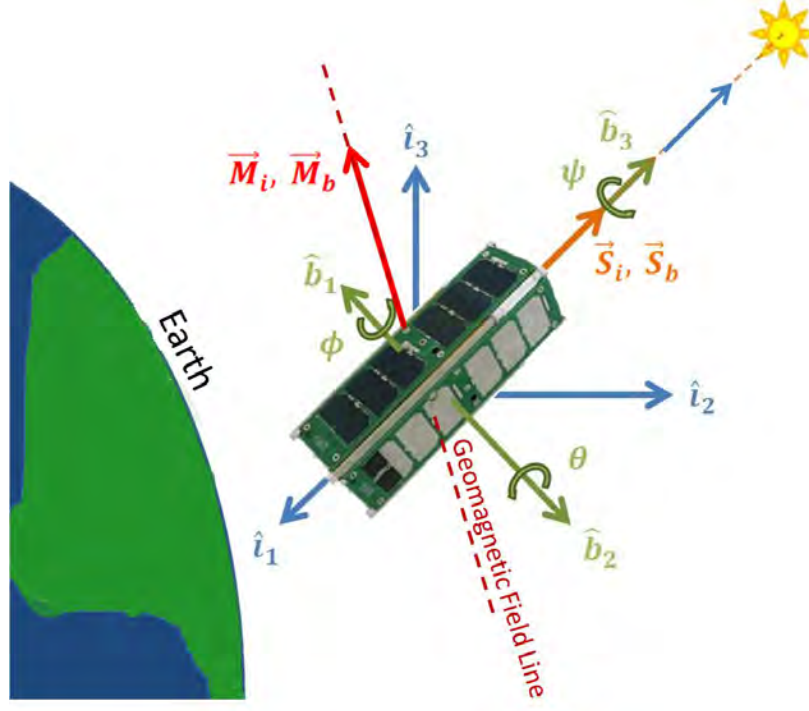


Figure 2.13: Magnetic and Sun Vectors in the Body and Inertial Reference Frames

Two orthonormal triads of vectors are generated from the Sun and magnetic unit vectors as shown in Eqn (2.5) [13].

$$\begin{aligned}
\hat{v}_{i1} &= \hat{S}_i \\
\hat{v}_{i2} &= (\hat{S}_i \times \hat{M}_i) / |\hat{S}_i \times \hat{M}_i| \\
\hat{v}_{i3} &= \hat{v}_{i1} \times \hat{v}_{i2} \\
\hat{v}_{b1} &= \hat{S}_b \\
\hat{v}_{b2} &= (\hat{S}_b \times \hat{M}_b) / |\hat{S}_b \times \hat{M}_b| \\
\hat{v}_{b3} &= \hat{v}_{b1} \times \hat{v}_{b2}
\end{aligned} \tag{2.5}$$

In Eq. (2.5) the first inertial and body frame vectors \hat{v}_{i1} and \hat{v}_{b1} are based upon the more accurate of the two sensors typically resulting in a more accurate estimate of the attitude. In this case, it was assumed the Sun sensor was more accurate than the magnetometer. Also Eqn. (2.5) requires that the magnetic and Sun vectors are not parallel. Two proper orthogonal matrices are then defined from

$$\begin{aligned}
A &\equiv [\hat{v}_{b1} \ \hat{v}_{b2} \ \hat{v}_{b3}] \\
B &\equiv [\hat{v}_{i1} \ \hat{v}_{i2} \ \hat{v}_{i3}]
\end{aligned} \tag{2.6}$$

and the resulting direction cosine matrix to convert from the inertial to body frame is defined as

$$C^{bi} = AB^T. \tag{2.7}$$

Sensor measurements may not be simultaneous which can result in some error in the estimate of the attitude. It is suggested in [13] that a correction can be made which utilizes the spacecraft's calculated angular velocity to correct for the rotation which occurs between measurements.

2.6.2 Optimal Attitude Determination. In contrast to deterministic attitude determination, methods of optimal attitude determination find a direction cosine matrix A that minimizes the cost function proposed by Wahba of IBM's Federal

Systems Division in 1965 [14, 46]. The cost function is

$$J(A) = \sum_{i=1}^n a_i |\mathbf{b}_i - A\mathbf{r}_i|^2 \quad (2.8)$$

where $J(A)$ is the cost function minimized for A , a_i are positive weighting factors, $\{\mathbf{b}_i\}$ is a set of n unit vectors in the body frame, and $\{\mathbf{r}_i\}$ is the same set of unit vectors in the inertial reference frame [14, 16, 46]. The positive weighting factors a_i are typically calculated as

$$a_i = \frac{1}{\sigma_i^2} \quad (2.9)$$

where σ_i^2 is the measurement variance [16, 46].

Eqn. (2.8) can be rewritten as

$$J(A) = \sum_{i=1}^n a_i - \text{TR}(AB^T) \quad (2.10)$$

where

$$B = \sum_{i=1}^n a_i \mathbf{b}_i \mathbf{r}_i^T. \quad (2.11)$$

and minimizing Eq. (2.10) requires maximizing the trace of AB^T [16, 46].

Many algorithms have been developed to minimize Wahba's problem (Eq. 2.8). Commonly referenced algorithms include Davenport's q-method [14, 18] and QUEST [18, 47]. Both methods will be addressed in this chapter as well as the optimal quaternion estimation method solution proposed in [16]. Information on optimization and costs functions can be found in books such as [48, 49]; therefore, further in depth details will not be provided in this research.

2.6.2.1 Q-method. The q-method was published by Davenport in 1968 [14]. The q-method utilizes an updated cost function

$$J(\vec{q}) = \vec{q}^T K \vec{q} \quad (2.12)$$

where K is a 4 x 4 matrix defined as

$$\begin{pmatrix} S - \mathbb{I}\sigma & \mathbf{Z} \\ \mathbf{Z}^T & \sigma \end{pmatrix}$$

where \mathbb{I} is the identity matrix and

$$\begin{aligned} C &= AB^T \\ S &= C^T + C \\ \mathbf{Z} &= (C_{23} - C_{32}, C_{31} - C_{13}, C_{12} - C_{21})^T \\ \sigma &= \text{TR}(C). \end{aligned} \tag{2.13}$$

Maximizing the new cost function includes the constraint that $\vec{q}^T \vec{q} = 1$. The cost function is again updated with a Lagrange multiplier and the addition of the constraint yielding

$$J(\vec{q}) = \vec{q}^T K \vec{q} - \lambda \vec{q}^T \vec{q} \tag{2.14}$$

where λ is the Lagrange multiplier as seen in many optimization problems. The new cost function is differentiated with respect to \vec{q}^T and set equal to zero resulting in

$$K \vec{q} = \lambda \vec{q} \tag{2.15}$$

which is a classical eigenvalue problem. The original solution was to maximize AB^T and now the largest eigenvalue of K maximizes the cost function. The corresponding eigenvector is the least-squares optimal estimate of the attitude as represented in quaternions [14,18]. If at least two of the body reference frame vectors, and identically the inertial vectors, are not collinear then the eigenvalues of K are distinct. The q-method can be computationally intensive making it difficult to use for on-board attitude determination [14].

2.6.2.2 QUEST. QUEST, or the Quaternion Estimation Algorithm was proposed by Schuster in 1978 as a method for finding the largest eigenvalue and corresponding eigenvector of the \mathbf{K} matrix as described in Sec. 2.6.2.1 that is less computationally intensive than the q-method. After some substitutions as described in [18] in the cost function, Wahba's problem condenses to

$$\lambda_{opt} = \sum_{i=1}^n a_i - J \quad (2.16)$$

where λ_{opt} is the optimal eigenvalue, a_i are the weighting values for the individual measurement vectors, and J is the cost function. The optimal eigenvalue is achieved by minimizing the cost function to essentially zero yielding

$$\lambda_{opt} \simeq \sum_{i=1}^n a_i. \quad (2.17)$$

After solving for the optimal eigenvalue the quaternion is computed by first solving for the 3 x 1 Rodriguez parameters p where

$$p = [(\lambda_{opt} + \sigma)\mathbb{I} - S]^{-1}\mathbf{Z} \quad (2.18)$$

where σ , S , and \mathbf{Z} are described in Eqn. (2.13).

After solving for the Rodriguez parameters the quaternion is calculated from

$$\vec{q} = \frac{1}{\sqrt{1 + p^T p}} \begin{bmatrix} p \\ 1 \end{bmatrix} \quad (2.19)$$

Singularities in the Rodriguez parameters occur when the rotation is of π radians [18], [47]. One method of resolving this issue is to set the quaternion to $\{0, 0, 0, 1\}^T$ when $p^T p$ is equivalent to -1 [47].

2.6.2.3 Optimal Fast Quaternion Estimation Algorithm. The optimal fast quaternion estimation algorithm, hereafter referred to as OFQEA, as described

in [16] proposes a method for estimating quaternions and in [16] it is demonstrated that OFQEA is a more accurate method of attitude estimation than the TRIAD method in simulated test scenarios. The OFQEA utilizes measurements from two sensors to calculate the satellite's attitude similarly to TRIAD. Unlike TRIAD, OFQEA minimizes Wahba's loss function hence the optimal terminology.

Again, as an example, a Sun sensor and a magnetometer will provide data in the body frames \vec{S}_b and \vec{M}_b and this data will be paired with knowledge of the Sun vector and magnetic field in the inertial frame \vec{S}_i and \vec{M}_i , respectively. A third vector in the inertial and body frame are calculated as

$$\begin{aligned}\hat{v}_{i3} &= (\vec{S}_i \times \vec{M}_i) / |\vec{S}_i \times \vec{M}_i| \\ \hat{v}_{b3} &= (\vec{S}_b \times \vec{M}_b) / |\vec{S}_b \times \vec{M}_b|.\end{aligned}\tag{2.20}$$

A normalized third vector in both the inertial and body frames is therefore created from the two inertial and two body vectors respectively. However, it is important to note that the Sun vector and magnetic vector cannot be collinear else there is not a unique solution to Eq. (2.20). The optimized quaternion estimation is based upon finding the principle Euler angle ϕ that can minimize Wahba's cost function. The resultant optimized quaternion is calculated via

$$\begin{aligned}q_{est} &= \frac{1}{2\sqrt{\gamma(\gamma + \alpha)(1 + \hat{v}_{b3} \cdot \hat{v}_{i3})}} \begin{bmatrix} (\gamma + \alpha)(\hat{v}_{b3} \times \hat{v}_{i3}) + \beta(\hat{v}_{b3} + \hat{v}_{i3}) \\ (\gamma + \alpha)(1 + \hat{v}_{b3} \cdot \hat{v}_{i3}) \end{bmatrix}, \alpha \geq 0 \\ q_{est} &= \frac{1}{2\sqrt{\gamma(\gamma - \alpha)(1 + \hat{v}_{b3} \cdot \hat{v}_{i3})}} \begin{bmatrix} (\beta(\hat{v}_{b3} \times \hat{v}_{i3}) + (\gamma - \alpha)(\hat{v}_{b3} + \hat{v}_{i3})) \\ \beta(1 + \hat{v}_{b3} \cdot \hat{v}_{i3}) \end{bmatrix}, \alpha \leq 0\end{aligned}\tag{2.21}$$

where

$$\begin{aligned}\alpha &= (1 + \hat{v}_{b3} \cdot \hat{v}_{i3})(a_1 \hat{S}_b \cdot \hat{S}_i + a_2 \hat{M}_b \cdot \hat{M}_i) + (\hat{v}_{b3} \times \hat{v}_{i3}) \cdot (a_1 \hat{S}_b \times \hat{S}_i + a_2 \hat{M}_b \times \hat{M}_i) \\ \beta &= (\hat{v}_{b3} + \hat{v}_{i3}) \cdot (a_1 \hat{S}_b \times \hat{S}_i + a_2 \hat{M}_b \times \hat{M}_i) \\ \gamma &= \sqrt{\alpha^2 + \beta^2}\end{aligned}\tag{2.22}$$

where a_1 and a_2 represent positive weight values used in the optimization process. If \hat{v}_{b3} is equal to $-\hat{v}_{i3}$, then the equation for q_{est} becomes indeterminate, or $0/0$. This is resolved by solving for the attitude with respect to an inertial coordinate frame related to the initial inertial reference frame by a 180° rotation about the X , Y , or Z axis. Solving for one of the quaternions with respect to the new inertial coordinate system yields

$$\vec{\mathbf{q}}^i = \begin{bmatrix} q_4 \hat{\mathbf{e}}_i - \mathbf{q} \times \hat{\mathbf{e}}_i \\ -\mathbf{q} \cdot \hat{\mathbf{e}}_i \end{bmatrix} \text{ for } i = 1, 2, 3 \quad (2.23)$$

where $\vec{\mathbf{q}}^i = \{q_1, q_2, q_3, q_4\}^T$, $\mathbf{q} = \{q_1, q_2, q_3\}^T$, and $\hat{\mathbf{e}}_i$ is a unit vector along the i^{th} axis such as $[1, 0, 0]^T$ if calculating a quaternion with respect to the new inertial axis based upon a rotation about the 1 axis [16].

2.7 Summary

Chapter II covered the background information on the use of simulated satellites for testing satellite components and software on Earth, attitude sensors, and the geomagnetic field. The theory behind Helmholtz coils and cages was presented in Chapter II as well as several examples of Helmholtz cages. Finally a discussion of deterministic and optimal attitude determination algorithms was provided. Information from Chapter II is utilized next in Chapter III in the design and build of the AFIT Helmholtz cage as well as in the selection and implementation of the optimal fast quaternion estimation algorithm (OFQEA).

III. Methodology

3.1 *Introduction*

Chapter II provided the background information of attitude sensors, the geomagnetic field, Helmholtz coils and cages, and attitude determination methods that lead up to the design of AFIT's Helmholtz cage and implementation of an attitude determination algorithm on the test CubeSat. Chapter III will cover the following:

- Design and build of the AFIT Helmholtz cage,
- Dynamic control of the cage,
- Test setup for cage testing,
- CubeSat attitude determination components used in this research effort, and
- Selection and testing of the optimal fast quaternion algorithm (OFQEA).

The first section introduces the calculations performed to determine the number of turns per coil and the sizes of the coils as well as how the cage was built. The second section covers hardware that accompanies the cage including the power supplies, truth magnetometer, test stand, and a stand for flashlights which simulate the Sun as a point light source. The third section covers the test setup used in testing the Helmholtz cage. The fourth section describes briefly the Sun sensor and magnetometer utilized on the test CubeSat. The final section covers the reason behind selecting the OFQEA over other algorithms, how the algorithm is coded, and how OFQEA is tested.

3.2 *Cage Design*

The goal in the design of the cage is to produce magnetic fields of $\pm 2\text{G}$ similar to the goal proposed by the University of Michigan (U-M). The COTS, U-M, and TU Delft cages all were approximately $2\text{ m} \times 2\text{ m} \times 2\text{ m}$ as discussed in Chapter II. Larger cages result in larger possible homogenous fields, so in the highly possible instance that a CubeSat with a deployable boom or a larger satellite was going to be tested in the cage it would be worthwhile for AFIT to possess a larger cage. Initial outer

dimensions were estimated to be 8' x 8' x 8' where 8' is approximately 2.4 m. English units are utilized over metric units as the aluminum 80/20 on-hand is cut in rounded English units. When the cage dimensions were tested in a Mathematica demonstration for Helmholtz Coils [50] the resulting uniform field in all three directions was approximately 30 cm as shown in Fig. 3.1. As 30 cm should provide a large enough area for most CubeSat testing, the 8' x 8' x 8' design was acceptable.

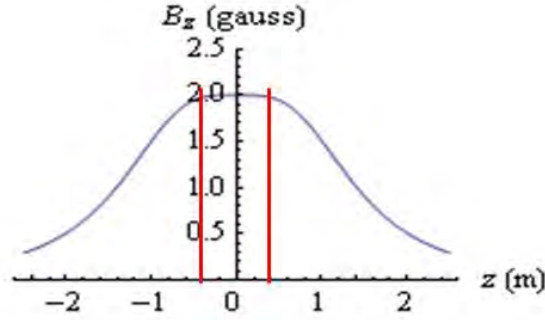


Figure 3.1: Estimated Uniformity of Generated Magnetic Field

The outer support structure of the cage is made from 1.5" 80/20 aluminum. The coils consist of 12 AWG Thermoplastic High Heat-resistant Nylon (THHN) coated wire wrapped around 1.5" aluminum U-channel. The corners consist of a plastic inner-piece with a 4" radius and an aluminum side piece for the right and left sides of the plastic to provide additional stiffness. The corner pieces are shown in Fig. 3.2.

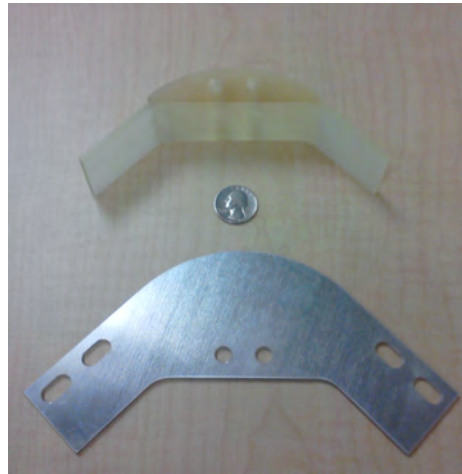


Figure 3.2: Corner Piece Components

The outermost coil is 92" from outer edge to outer edge providing 0.5" of leeway on either side for support brackets. The next coil is 89" from outer edge to outer edge so that it nests within the outer coil. The smallest coil is also designed to nest within the other two coils and therefore is 86" from edge to edge thus the coils have lengths of 92", 89", and 86".

Three HP 6038A power supplies (PS) supply a wide range of capabilities of 0-60 V and 0-10 A at 200W. The coils are designed with these PS capabilities in mind and with the assumption that 200W is a limiting factor. From Eqn. (2.4), which is used to calculate the magnetic field generated by square coil pairs and a standard resistance for 12 AWG copper wire of 1.588 Ohms/k-ft or 1.32E-4 Ohms/in, the resulting number of turns for each coil is 54. With this information, magnetic fields of +2 G could theoretically be generated with 5.32 A and 27.98V for the largest coil pair, the middle size coil pair would require 5.15 A and 26.2 V, and the smallest coil pair would require 4.98 A and 24.48 V.

The coils were wrapped by placing a spool of wire on a turntable on top of a wooden box and while one of the assembled U-channel pieces was placed on another turntable on another wooden box. First, a layer of electrical tape was wrapped around the U-channel to add friction and ensure that the wire could not be pinched by the corners at the junction between the plastic corner and U-channel. Then two individuals manned the U-channel in order to lay the wire in neat rows while another individual manned the spool of wire providing tension between the coil and the spool. Once the coil had 54 wrappings the coil was then wrapped again with electrical tape. The intent was to lay the wire in neat rows so that the magnetic field was completely perpendicular to the flow of current, however this proved to be very difficult with 12 gauge wire. Assuming a worst case scenario where a wire at the bottom of the wrapping of the smallest coil touches the left side of the U-channel on one end and the right side at the other end the maximum angle offset of the magnetic field from the plane of the coil is 0.86° . Therefore, the net direction of the generated magnetic field is not greatly impacted and since the wrapping process was very labor intensive

and counted on the assistance of volunteers it was decided that it was not worth the effort to lay the coils in absolutely neat rows. The wire also bows out slightly at the mid-point of the U-channel due again to the thickness of the wire and the difficulty in wrapping the coil. The turntables with the mounted spool of wire and aluminum U-channel are shown in Fig. 3.3.

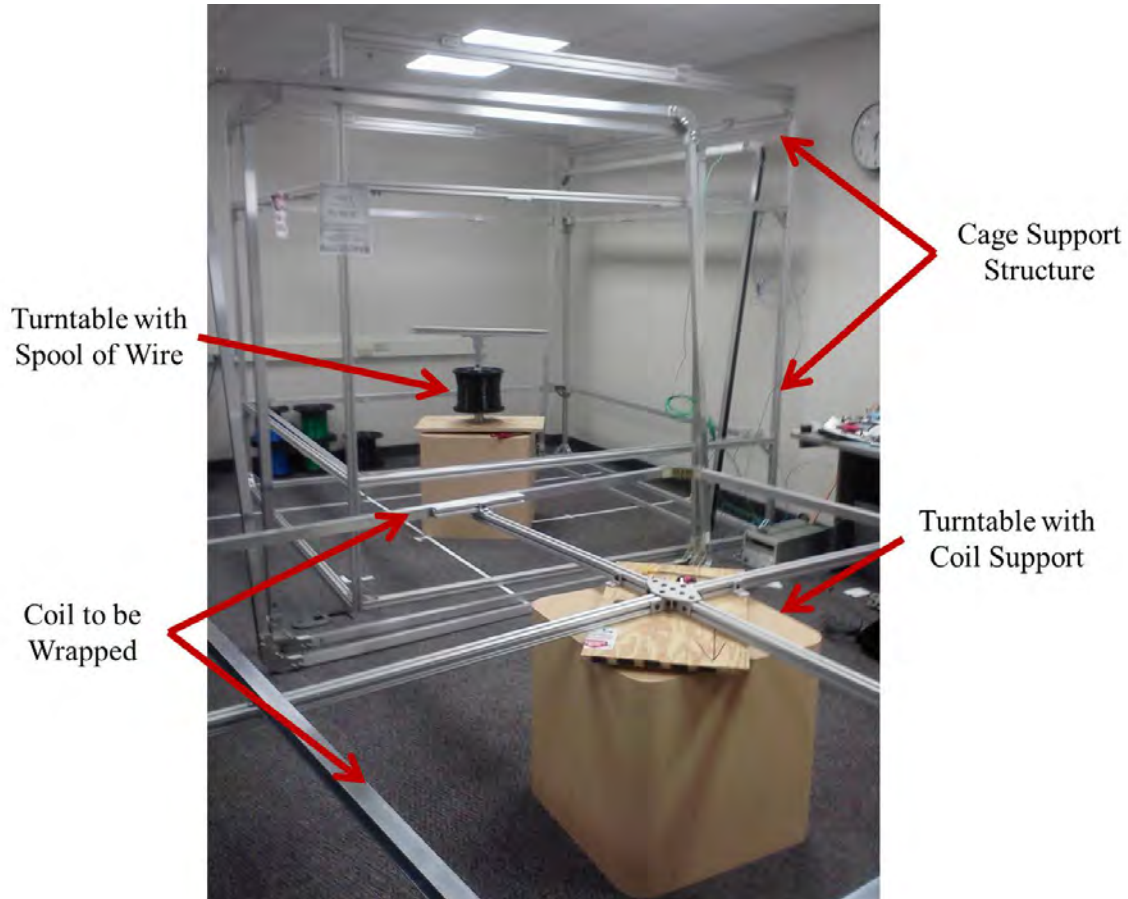


Figure 3.3: Coil Wrapping Configuration

The wrapped coils were installed into the cage in a certain orientation based on several factors. First and foremost was the consideration of the ambient magnetic field at the proposed cage location. The geomagnetic field is commonly defined with +X pointed North, +Y pointing East, and +Z pointing down. The cage axes were selected to match this definition. The final design requires that all supports be made from plastic to electrically isolate the coils from the support structure; however, aluminum with steel fasteners was used as an intermediary as can be seen in Fig. 3.4. The coils

controlling the Z axis are the largest coils in order to minimize deflection of a plastic support piece with time. The next consideration involved the X or North component of the ambient magnetic field which is larger than the Y or East component. If the direction of the X component needed to be reversed a higher magnitude magnetic field would be required than that required to flip the Y direction magnetic field. Larger magnetic fields are generated by smaller coils thus the smallest coil was selected to control the X direction. Therefore, the remaining middle sized coil controls the Y direction. The final cage is shown in Fig. 3.4.

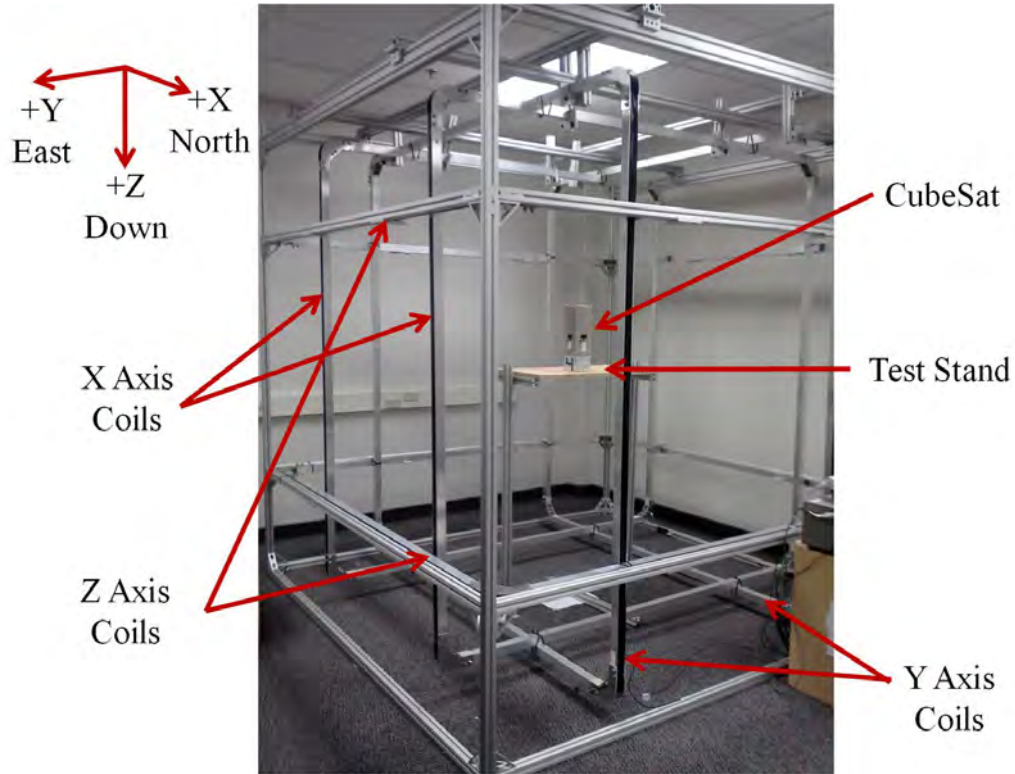


Figure 3.4: AFIT Helmholtz Cage

Eqn. (2.4) relies on the coils being orthogonal, centered, and properly spaced. Therefore, the coils are spaced apart according to the Helmholtz spacing ratio of 0.5445 described in Sec 2.4. The nested coils are secured to each other with zip ties not only stabilizing the structure but also straightening some of the coils as they had warped during the wrapping process. The coils are secured to the outer support structure via zip ties as well for the same reasons.

3.3 *Cage Equipment*

This section describes equipment that accompanies the Helmholtz cage. Items discussed include the power supplies, light source, test stand, switch relays, and a control computer.

3.3.1 Power Supplies. As previously mentioned, the original design was based around using three HP 6038A power supplies (PS) capable of 0-60 V and 0-10 A at 200 W. At the time of testing one of the PSs did not work so it was replaced with a HP 6033A PS capable of 0-20 V and 0-30 A and 200W. Changing to the PS with lower available voltage affects the ability of the cage such that a magnetic field of ± 2 G in the Y direction is not achievable as discussed in Sec. 4.2.1. However, all three power supplies are still capable of GPIB control. The non-functioning PS was sent for repair and can be implemented in the design once repaired.

3.3.2 Truth Magnetometer. A 3-axis mG meter from AlphaLab, Inc. was selected as the truth magnetometer for the cage. The magnetometer is capable of measuring magnetic field up to ± 2 G. 3.6. Magnetic fields above this value do not damage the sensor; however, the data is no longer considered valid and the digital display does not provide data. A 2 meter cable connects the 1.5" x 1" x 1" sensor to the display module. The module has 3 BNC outputs for outputting voltage data which can be transformed to Gauss with the conversion of 1 V/G [39]. The 3-axis magnetometer has been successfully connected to MATLAB via 3 BNC cables with a BNC to USB module. The same magnetometer is utilized by the Delft University of Technology [9].

3.3.3 Light Source. Testing of the attitude determination algorithm requires a light source acting as the Sun. Several flashlights attached to a stand serve as the source of light. The stand height is adjustable so that the flashlights can be raised or lowered and the stand is not attached to the cage and can be moved anywhere.

3.3.4 Test Stand. A test stand was made out of 80/20 aluminum and plywood. The stand can be adjusted to various heights and can be moved anywhere within the cage. Before each test the platform was checked with a level to ensure that it was coincident with the X/Y plane of the cage. The stand is shown in Fig. 3.5.



Figure 3.5: Test Stand

3.3.5 Relays. Double Pole Double Throw switch relays were ordered to provide the ability to switch the direction of the magnetic field rather than having to disconnect and switch the coil leads when necessary. As designed, one relay can operate one pair of coils. The selected relays are capable of relaying 8 A and 30 VDC which is just high enough to enable ± 2 G fields in all 3 directions. The relays require a 6 VDC PS to operate. Sockets were also ordered to accompany the relays and provide the connection terminals between the coils and power supplies. A PS was selected to command the relays and the relays should be installed as future work. The PS should be connected to the control computer described in Sec. 3.3.6 so that

the relays can be utilized in the closed-loop control of the cage as described in Sec. 3.4.

3.3.6 Control Computer. A laptop equipped with MATLAB, Satellite Tool Kit (STK) with the Space Environment and Effects Tool (SEET), and LabVIEW is used to control the AFIT Helmholtz cage. MATLAB was used to perform closed-loop control of the magnetic field of the cage based on geomagnetic data from STK/SEET. LabVIEW was used for initial communication with the truth magnetometer and PS. Although LabVIEW is not utilized for any form of control, it was very useful for obtaining device addresses and ensuring that communication with the truth magnetometer and PS was possible.

3.4 Cage Control with STK

The cage is capable of simulating the magnetic field environment a satellite would experience on orbit. The cage is currently set to model a satellite operating in a 300 km circular orbit at an inclination of 28° . STK is used to generate a listing of time and 3-axis magnetic field values from the provided orbital parameters. A special report format for STK was created and saved which generates a report listing only the time and magnetic field in the +X North, +Y East, and +Z Down direction in mG utilizing information from SEET associated with STK. The length of the report will be the start and stop time of the scenario however this can be modified either in MATLAB or STK. The closed-loop control of the magnetic field is represented by Fig. 3.6 and described in the remainder of this section.

A MATLAB script commands the power supplies according to the desired magnetic field as per the SEET report all while responding to feedback from the truth magnetometer. When run, the script will connect with STK via STK Connect via the *stkInit*, *stkOpen*, and *stkExec* commands. MATLAB will then call for STK to set the magnetic field properties of the satellite in the scenario to utilize the Main Field IGRF and External Field Olson-Pfitzer data as discussed in Sec. 2.3.2. Then,

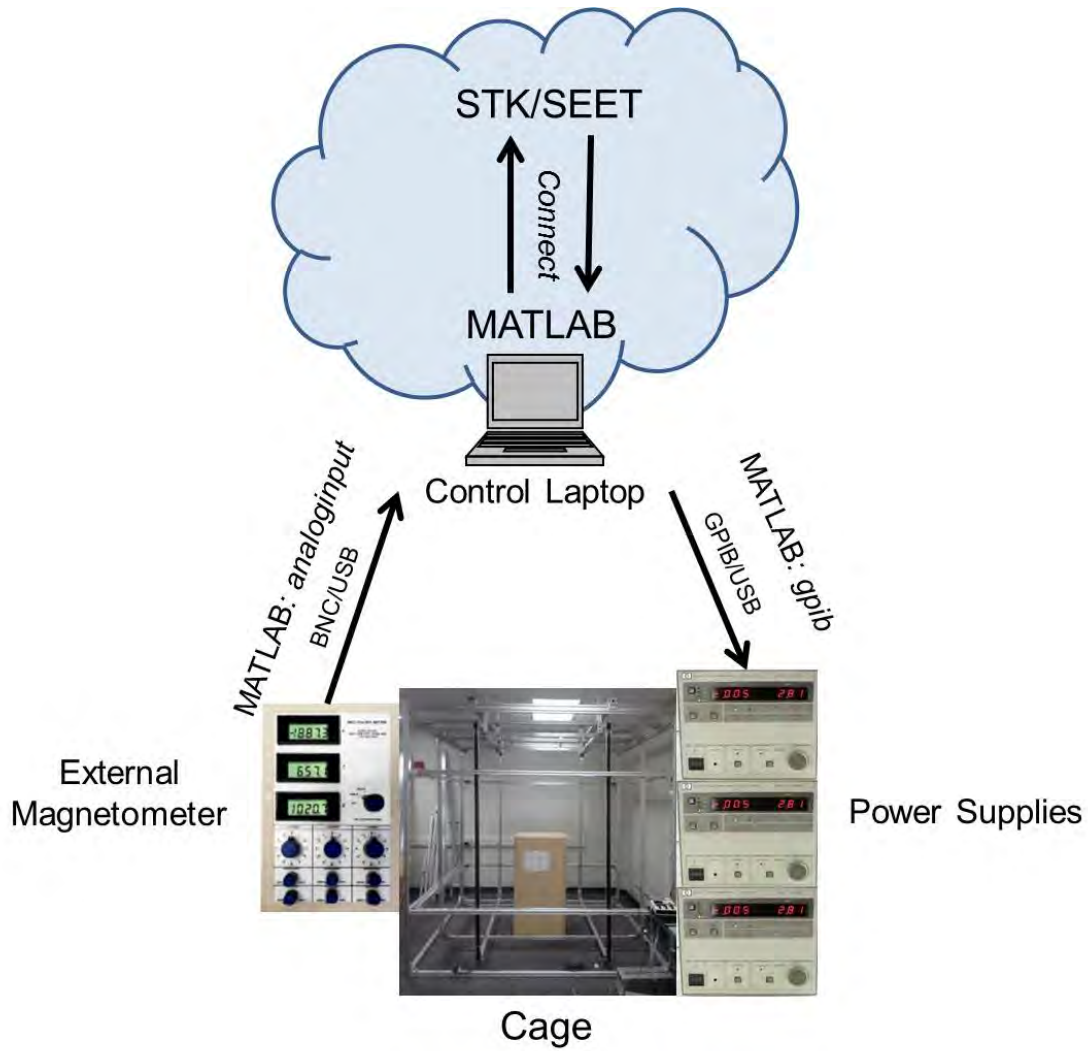


Figure 3.6: Closed-Loop Control of the Magnetic Field

the dynamic control script requests and saves a report of the geomagnetic field the satellite in the scenario would experience based on the special report format.

Next the dynamic control script connects to the power supplies via the MATLAB *gpib* command. The power supplies are daisy chained and connected to the laptop via a GPIB to USB component. The first action performed is to set the voltage on the power supplies to maximum so that the power supplies remain in constant current (CC) mode during operation. The initial setting of the voltage does not actually command this output voltage, instead it ensures the PS remains in CC mode. If

the voltage were set at a low value and the current became high enough that a higher voltage was necessary, the PS switches to constant voltage (CV) mode where *gpib* inputs should be in Volts not Amps. The dynamic control script functions by commanding the current, not the voltage, which is why it is important to stay in CC mode. The PS addresses are 1, 9, and 5 for the power supplies controlling the X, Y, and Z components, respectively. The addresses must all be different for the *gpib* command to work and the address cannot match the address of the GPIB board. The GPIB board address used in this design is 0.

The dynamic control script then connects to the truth magnetometer over a BNC/USB connection via the *analoginput* command in MATLAB and an initial reading of the ambient magnetic field at the truth magnetometer location is stored for use in further operations. The initial reading is based on the average of 100 data samples and the magnetometer output is 1 Volt per Gauss. The output is finally multiplied by 1000 to convert the data to mG

After storing the initial ambient magnetic field and several constants utilized in Eqn. (2.4), The MATLAB script runs through a ‘for’ loop which finds the difference between the desired magnetic field as calculated in STK and the initial ambient magnetic field. The necessary current to achieve that difference is then back calculated from Eqn. (2.4). MATLAB will then command the current and verify with the truth magnetometer that the desired magnetic field was achieved. If not, the script will run through several ‘while’ loops until the magnetic field is achieved within a certain tolerance. Once the desired magnetic field is achieved the script moves to the next desired magnetic field at the next time step.

When the switch relays are installed, the script will have to be modified slightly. The standard ambient magnetic field at the center of the cage in the X direction is the average value of the magnetic field a satellite would experience on orbit. As such, the magnitude increases and decreases around this average value, therefore requiring a change in the polarity of the current running through the X coil. Performing this

increase and decrease is not possible in the current configuration without switch relays. To solve this issue the desired magnetic field in the X direction is multiplied by negative one in the MATLAB script so that commanded field does not fluctuate around the ambient X component. An analysis of the cage's capability to simulate the on-orbit magnetic field is provided in Sec. 4.2.3.

3.5 Cage Test Setup

This section discusses two tests that were performed before the cage was built: an analysis of the effects of objects on the ambient magnetic field and a survey of the geomagnetic field in the proposed location for the cage. Also discussed is an analysis of the expected generated magnetic field and how the ability of the cage to zero the ambient magnetic field was tested across the test plane.

3.5.1 Object Influence on Magnetic Field. Before building the cage it was important to understand how the magnetic field is affected by different objects prevalent in the classroom where the cage was going to reside. The truth magnetometer remained in one location as a control while different objects were brought closer to the magnetometer in an effort to see at what distance the magnetic field recorded by the magnetometer would change. Results are provided in Sec. 4.1.1.

3.5.2 Room Survey. The second test involved surveying the magnetic field in the proposed area for the cage. A system of three magnetometers was used to characterize the magnetic field in the area. The three magnetometers fastened with plastic screws to a wood shelf and attached to a plastic cart can be seen in Fig. 3.7.

Discrete data was collected for at least 10 seconds with 1 second time intervals for all three magnetometers simultaneously. All three magnetometers were then rolled to a different location and the data collect was repeated. Data was collected from 1000 to 1500 local on the 11th of November 2011 and 1500-1700 on the 15th of the same



Figure 3.7: Three Magnetometer System

month in order to minimize diurnal changes. The collected data was then averaged, normalized, and plotted in MATLAB and is shown in Sec. 4.1.2.

3.5.3 Expected Generated Magnetic Field. The expected magnetic field at the center of the cage is calculated by adding the ambient magnetic field to the expected generated magnetic field from Eq. (2.4). AWG charts provide an average resistance of 1.588 Ohms/k-ft or $1.32\text{E-}4$ Ohms/in for 12 gauge copper wire. The expected magnetic field at the center of the cage for an ambient magnetic field of 230.7 mG, -105.5 mG, and 433.2 mG in the X, Y, and Z directions respectively in a cage with 54 wrappings per coil and coil dimensions of 92", 89", and 86" is provided in Table 3.1. The final relation between applied current and magnetic field is provided in Sec. 4.2.1.

Table 3.1: Expected Magnetic Field

Coil	Current (A)	Magnetic Field at Cage Center (G)
X (85")	0.565	0
Y (88")	0.269	0
Z (91")	1.14	0
X (85")	5.475	-2
Y (88")	4.08	1.5
Z (91")	6.39	-2

3.5.4 Zeroing the Ambient Magnetic Field. Testing of the ability of the cage to zero the magnetic field across a test plane was performed by zeroing the magnetic field at approximately the center of the test plane and running a truth magnetometer over the plane at 1.5” intervals as shown in Fig. 3.8.

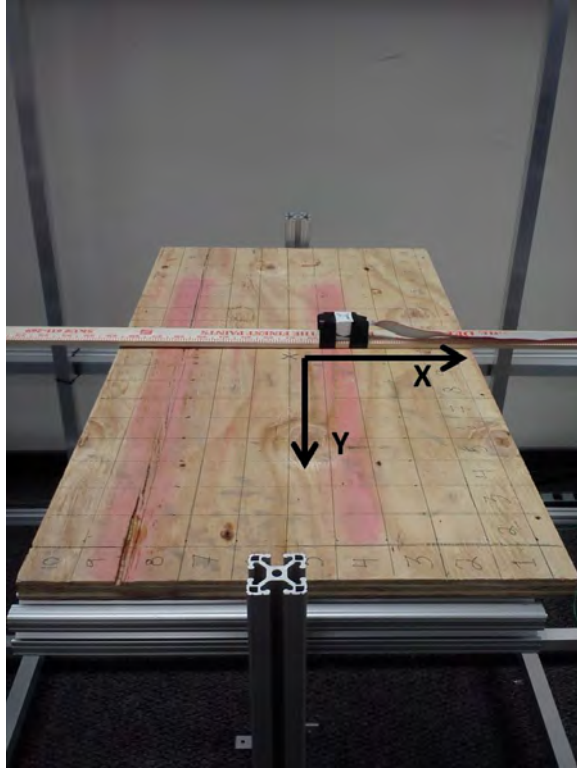


Figure 3.8: Test Plane

The axes displayed in Fig. 3.8 are representative of the center point or origin of the cage. The magnetic field was tested across 10 different locations in the X direction and 19 locations along the Y direction for a total of 190 test points. The tested area is approximately 15” by 28.5”. Results are provided in Sec. 4.2.2.

3.6 *CubeSat Components*

The CubeSat used in this experiment is commanded and controlled via the Arduino Mega board that is based on the ATmel ATmega1280 microcontroller which is used on the C&DH and EPS boards on the test CubeSat. Communication between

the Mega board and the Arduino integrated development environment (IDE) running on a laptop can either be via hardline with USB or wirelessly over an Xbee Radio. The CubeSat has its own batteries and EPS. The CubeSat also has light sensors and a magnetometer for attitude determination as well as reaction wheels for attitude control. The light sensors and magnetometer will be discussed further in this section.

3.6.1 Sun Sensors. The CubeSat is equipped with six Vishay TEMT6000 ambient light sensor breakout boards similar to Sun presence sensors as discussed in Sec. 2.2. The light sensors act as Sun sensors for attitude determination and the sensors are shown in Fig. 3.9.

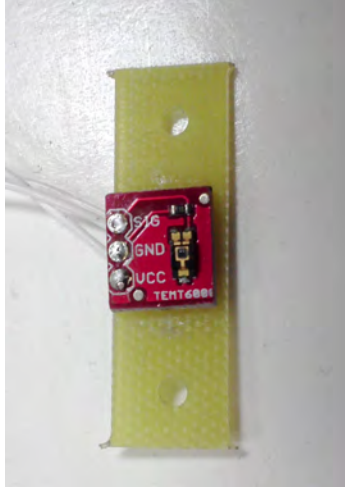


Figure 3.9: TEMT6000 Light Sensor

One Sun sensor is located on each face of the CubeSat at the approximate center of each face. Because a 10-bit A/D converter is used, the light sensors are capable of outputting values of 0 for no light detected to a maximum of 1024 when a light source is placed directly over the sensor. The light sensors are used to calculate the Sun vector in the body frame of the CubeSat utilizing azimuth Az and elevation El angles as shown in Fig. 3.10.

The azimuth angle is calculated on-board the CubeSat in the Arduino environment via the *atan2* function utilizing the maximum Sun sensor value between the Sun sensor in the +X direction and the Sun sensor in the -X direction versus the

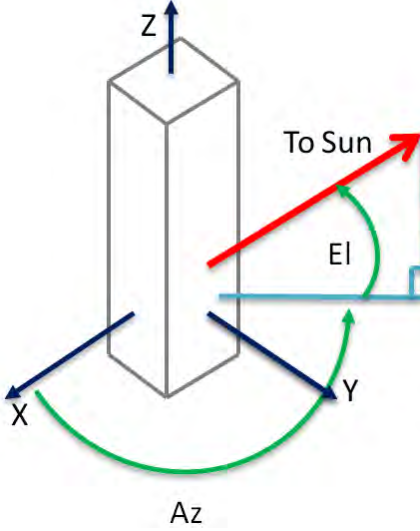


Figure 3.10: Sun Vector Angles in the CubeSat Reference Frame

maximum values for the sensor in the $+Y$ direction and $-Y$ direction. The elevation angle also utilizes the *atan2* function with the maximum value from the positive and negative Z direction sensors versus the horizontal component of the Sun vector as calculated from data from the X and Y Sun sensors. A Sun sensor must be placed at the middle of a face to ensure the proper geometry for these calculations. The light sensors also have a different relative radiant sensitivity when the light is off boresight as compared to when the light is nadir; however this information was not taken into account in the computation of the Az and El angles. Recommendations for future work include incorporating the radiant sensitivity of the Sun sensors to improve the accuracy of the sensor.

3.6.2 Magnetometer. Like the Sun sensors, a magnetometer is also used for attitude determination. As mentioned in Sec. 2.2 the magnetometer on-board the CubeSat is a HMC5843 3-Axis Digital Compass IC from Honeywell on a SEN-10183 9 degrees of freedom (DOF) board available from Sparkfun. The front and back of the 9 DOF board is shown in Fig. 3.11 where the magnetometer is the black component in the middle of the board.

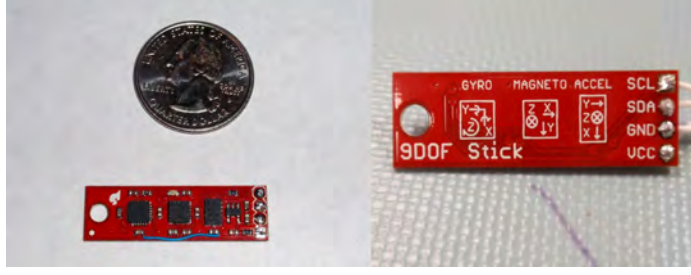


Figure 3.11: Sparkfun 9 DOF Board

Raw data from the magnetometer can be pulled from the 9DOF board into the Arduino environment using the standard HMC library from Arduino. Testing of the magnetometer will be described further in Sec. 4.3 including the offset and linearity of the magnetometer as well as effects of the reaction wheels. The magnetometer operates for magnetic fields of ± 4 G as per the spec sheet [24].

3.6.2.1 Magnetometer Placement. Precise attitude determination when using only Sun sensor and magnetometer data is highly dependent upon the accuracy of the magnetometer so much consideration needs to go into its placement. The on-board magnetometer was initially installed on the C&DH card of the CubeSat. The CubeSat was placed next to the truth magnetometer with the on-board and truth magnetometers at the same height and no greater than a centimeter apart. The magnetic magnitudes in all three directions of the truth magnetometer would vary up to 50 mG in a magnetic field environment of 1.5 G, and if the CubeSat was removed, the readings of the truth magnetometer would return to normal indicating that there was a magnetic field being generated by the CubeSat. The CubeSat was then disassembled and the reaction wheel assembly with ADCS card and then each individual card was placed next to the truth magnetometer to check the component's effect on the magnetic field.

The majority of cards as well as the reaction wheel assembly had a minimal effect on the truth magnetometer of no greater than 3 mG. The C&DH card however caused changes in the magnetic field of 50 mG as experienced when the entire assembly was placed next to the truth magnetometer. The C&DH card had a low resistance

circuit which carried a current in the 1.5 G environment producing a magnetic field. The CubeSat was capable of providing telemetry in the 1.5 G environment so testing proceeded with the assumption that the increased current in the circuit was not affecting any vital component. However, the on-board magnetometer was moved to the end of the CubeSat the furthest distance from the C&DH card to prevent any interference from the induced magnetic field. The truth magnetometer at the elevation of the new magnetometer was not affected by more than 3 mG when the newly located on-board magnetometer and CubeSat assembly was placed next to the truth magnetometer. The orientation of the 9 DOF board with respect to the top of the CubeSat is provided in Fig. 3.12. The 9 DOF board is approximately in the center of the top face of the CubeSat set slightly within the CubeSat.

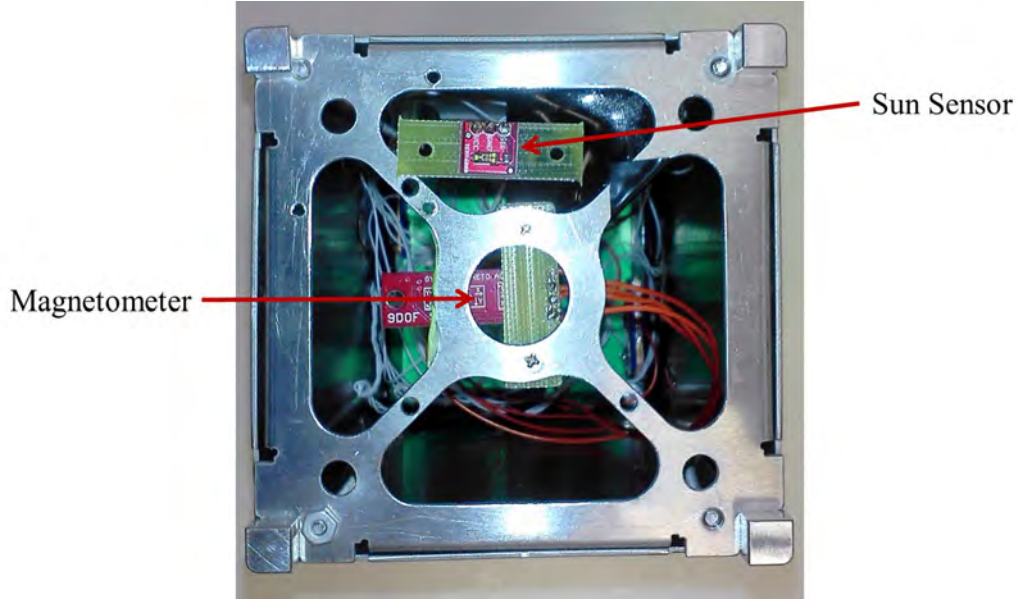


Figure 3.12: Final Placement of On-board Magnetometer

3.7 *CubeSat Attitude Determination Algorithm and Testing*

The final topic covered in Chapter III is the implementation of the attitude determination algorithm and a description of how the algorithm was tested. Attitude determination is performed via the Arduino Mega board on the C&DH board on-board the CubeSat. The optimal fast quaternion estimation algorithm (OFQEA), as

described in Sec. 2.6.2.3, was selected for the CubeSat because it is an optimized algorithm compared to the TRIAD method as described in Sec. 2.6.1. It was also selected over the q-method and QUEST as described in Sec. 2.6.2.1 and Sec. 2.6.2.2 as the documentation on OFQEA provided an exact solution of the optimal quaternion that was not dependent upon calculating the eigenvalues and eigenvectors of the cost function. Coding the Arduino platform to calculate determinants and solve an eigenvalue problem is more difficult than coding dot products, cross products, and matrix multiplication as utilized by OFQEA.

The two vectors utilized in the OFQEA algorithm by the CubeSat are the Sun vector and the magnetic vector. The inertial Sun and magnetic vector are added directly into the code so that if the flashlight and cage magnetic field are changed these vectors also need to be changed. All of the body and inertial Sun and magnetic vectors are transformed into unit vectors. The sensors are equally weighted in the code to represent equal measurement variances in the sensors and an initial guess of 1 for each weight was utilized as there is no a priori knowledge of the variances. Both the estimated quaternions for α greater than 0 and α less than 0 are included in the code but the code does not currently handle the case when \vec{v}_{b3} is equal to $-\vec{v}_{i3}$.

During testing, the USB connection was always removed so that the control laptop could be outside of the cage and therefore not impact the magnetic field. The CubeSat transmitted telemetry over the Xbee radio during testing. Telemetry included raw data from the Sun sensors as well as raw data from the magnetometer. It also included the azimuth and elevation of the Sun vector as calculated by the Sun sensors, the estimated quaternions, and the Euler angles associated with a 1-2-3 rotation as calculated from the estimated quaternions.

Evaluating the attitude algorithm included testing with a magnetic vector of $\{0, 0, -2\}_i$ G and then $\{0, 1.5, 0\}_i$ G. The magnetic vector was verified by placing the truth magnetometer directly over the on-board magnetometer and then removing the truth magnetometer before beginning rotation of the CubeSat. In both cases, the

Sun vector was $\{1, 0, 0\}_i$. The location of the flashlights and test setup for attitude algorithm testing is depicted in Fig. 3.13.



Figure 3.13: Attitude Determination Testing with Illumination

During the testing, the CubeSat was rotated by hand on top of a compass rose on top of the test stand. The approximate direction was verified with a ruler from the mid-point of a face of the CubeSat as shown in Fig. 3.14. The CubeSat was checked via ruler after each rotation to confirm that it was still centered over the compass rose. Accuracy of the truth rotation via the compass rose is well within $\pm 1^\circ$. Results of the attitude determination testing with the magnetic field in the $-Z_i$ and then Y_i directions are provided in Sec. 4.4.

After performing the attitude determination tests, the raw data was stored and reused in MATLAB to validate a duplication of the OFQEA in MATLAB. Once validated, the accuracy was tested for different weights of 1 and 3 for the Sun sensors and magnetometer respectively and then vice versa. The results were then plotted against the equally weighted solution as calculated by the CubeSat. The results



Figure 3.14: Truth Rotation of CubeSat

are provided in Sec. 4.4.2. Finally, the raw data was used to compare the TRIAD method as computed via MATLAB simulation versus the OFQEA test data. Results are provided in Sec. 4.4.3.

3.8 *Summary*

Chapter III covered the design and build of the Helmholtz cage including the number of wrappings selected per coil and the dimensions of each coil. Also covered was the methodology for dynamically controlling the cage to simulate the on-orbit geomagnetic field via MATLAB and STK. The test configuration of all the testing discussed in Chapter IV was covered in Chapter III. The CubeSat was covered in further detail and the selection and implementation of OFQEA was discussed in detail.

IV. Results & Analysis

This chapter presents the results of the tests described in Chapter III. The results are analyzed and suggestions for improvement are provided accordingly. The first set of results covers an analysis of the affects of electrical and ferromagnetic objects on a magnetic field and then an analysis of the ambient magnetic field before the cage was built. The next set of results pertain to the Helmholtz cage as-built including its maximum and minimum magnetic field capabilities, the ability to zero the magnetic field across the test plane at the center of the cage, and the accuracy of the dynamic simulation of the geomagnetic field a CubeSat would experience in orbit. The third section covers the results of magnetometer testing including an analysis of the linearity and offset of the magnetometer as well as the impact, or lack thereof, of the reaction wheels on the magnetometer. The fourth and final section provides the results of attitude determination testing.

4.1 *Analysis of Ambient Magnetic Field Pre-Cage*

4.1.1 Effects of Electrical and Ferromagnetic Objects. To understand the ambient magnetic field it is important to understand the effects of objects prevalent in the local environment. The cage is in a lab classroom setting with ferromagnetic toolboxes, steel desks, and several computers. The distance at which different objects affect the magnetic field are provided in Table 4.1.

Table 4.1: Proximity Testing

Object	Distance (inches)
Pasco Rotary Sensor	15
Power Supply	5
Laptop	21
Metal Toolbox	51
Steel Desk	76

During testing the power supplies were tested when powered on as well as off which actually did not have an effect on the distance at which the magnetic field would change. The laptop was powered on and off during testing as well and there

was not a difference between the two, thus material properties, not electric currents are the dominant influence on the magnetic field. It was determined from the testing that the Pasco Rotary Sensor in the current configuration could not be used as the truth rotation device for attitude determination. The steel desks have the furthest reaching affect, but they are a necessity in the classroom and an aluminum desk is suggested for the immediate vicinity to house the control laptop and power supplies and the desks already in the classroom are arranged as best as possible to minimize the impact on the cage. Details on the setup for the test are provided in Sec. 3.5.1.

4.1.2 Room Survey. This section provides the results of a survey of the ambient magnetic field in the proposed area for the Helmholtz cage as described in Sec. 3.5.2. The results are provided in Figs. 4.1 and 4.2.

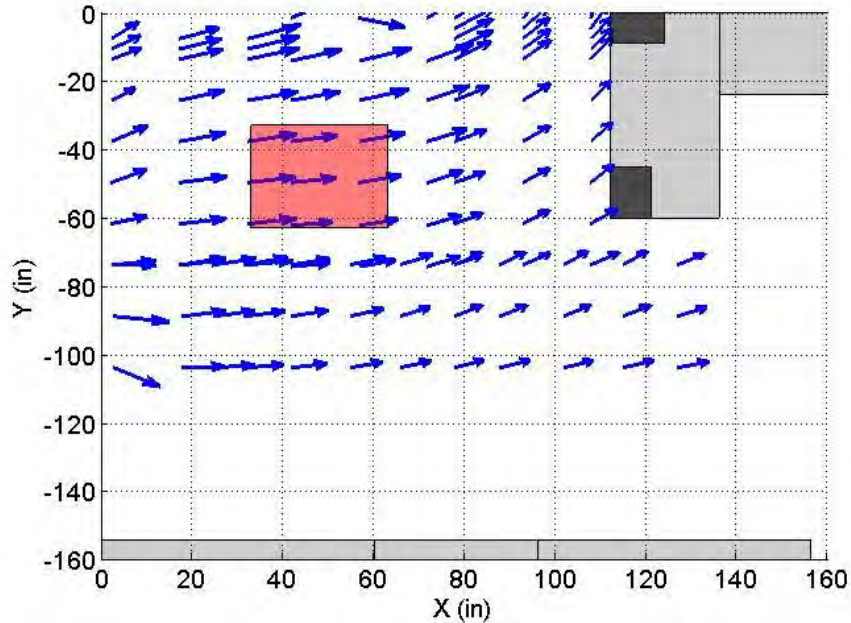


Figure 4.1: Ambient Geomagnetic Vector Pre-Cage

In Fig. 4.1, magnetic North is in the positive X direction and slightly positive Y direction. The units of the mapping are in inches. The long gray bar at the bottom of the figure represents a steel desk from 0" to 60", a toolbox from 60" to 98", and another desk from 98" to 158". Another steel desk is represented in gray at the top

right with the laptop used to collect data from the magnetometers at the bottom corner, represented in a darker gray, and a PC tower at the upper corner which is also represented by a darker gray block. Both the PC tower and laptop were on during testing. Another steel desk was perpendicular to this desk. There is a wall extending along the upper edge along the '0' Y locations and a wall along the left edge along the '0' X locations. The red square in the middle represents the expected location of the uniform field of the Helmholtz cage. As shown in Fig. 4.1, the wall had a minimal effect on the geomagnetic field when compared to the effects of the steel desk with the PC tower and laptop. The steel desk is composed of ferromagnetic material and as such displays the ability to greatly affect the geomagnetic field causing the field to rotate as it approaches the desk. This desk was therefore removed before building and testing the cage. Fig. 4.2 is a side view of Fig. 4.1 which exhibits the declination of the geomagnetic field for the room.

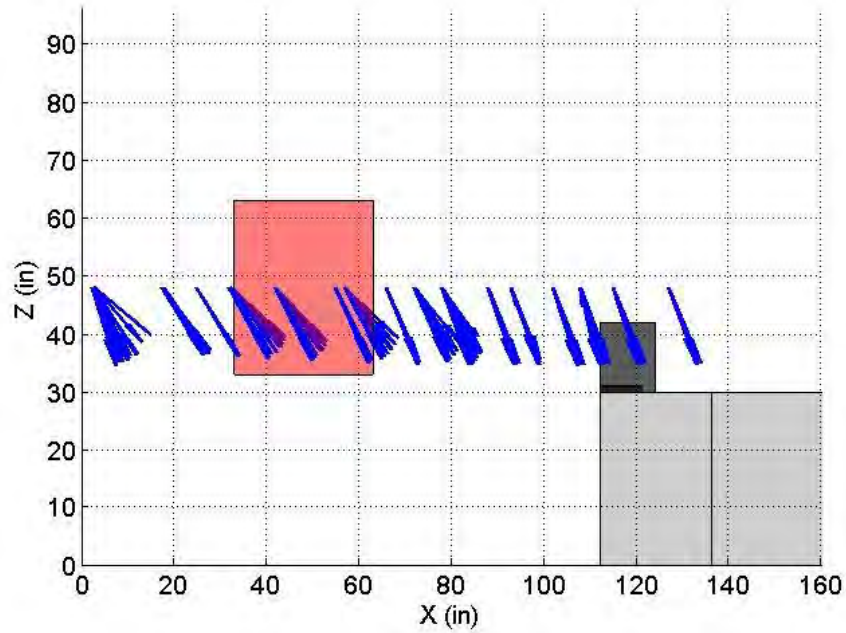


Figure 4.2: Ambient Geomagnetic Vector Pre-Cage Side View

As shown in Fig. 4.2, the geomagnetic field along the '0' X position has a varying declination with the field nearest the reader having the greatest declination on average compared to other vectors along the same X position. The same magnetometer was

not used for each vector along the back wall, ruling out error from a magnetometer. As the field vectors along the ‘20’ X position are fairly consistent, the difference in declination between the near and far vectors likely is not a function of the wall furthest from the reader. The wall to the left along the X axis had a cable conduit with active cables which likely is the source of the evident effect on the geomagnetic field closest to the wall. The declination of the field becomes more consistent as the field approaches the desk showing again that the desk has a strong effect on the local geomagnetic field.

4.2 *Helmholtz Cage Analysis*

4.2.1 Resultant Magnetic Field Capability. The measured capabilities of AFIT Helmholtz cage are provided in Table 4.2. Throughout this testing maximum field values were generated while holding the other axes at approximately 0 mG.

Table 4.2: Measured Magnetic Field Capability of AFIT Helmholtz Cage

Direction	Power Supply Settings	Resultant Field (G)
X	20.4 V 4.21 A	+1.999
X	27.3 V 5.62 A	-1.999
Y	20.4 V 3.96 A	+1.506
Y	20.5 V 3.92 A	-1.692
Z	21.5 V 4.29 A	+1.999
Z	31.8 V 6.23 A	-1.999

The AFIT Helmholtz cage is capable of changing the magnetic fields at the center of the cage to at least ± 2 G in the X and Z directions with the limitation being the ± 2 G range of the truth magnetometer. The ambient magnetic field at the center in the X direction was approximately +235 mG at the time of testing and the ambient magnetic field in the Z direction was +417 mG. The maximum abilities of the X and Z axis power supplies is 36.3 V with 7.52 A and 36.1 V with 7.25 A before overload, respectively. With these values the cage would theoretically be capable of generating magnetic fields of ± 3 G in addition to the ambient magnetic field. Both the X and Z axis coils utilize the Agilent 6038A power supplies. The Y axis coils utilize the HP/Agilent 6033A power supply with lower voltage ability than

the 6038A. Because of the lower voltage the Y axis coils are capable of changing the magnetic field at the center of the cage from -1.692 G to 1.506 G while maxing out the capabilities of the 6033A power supply at 20.5 V with 3.92 A and 20.4 V with 3.96 A, respectively.

The actual magnetic field generated by the cage is compared to the estimated generated magnetic field in Table 4.3. These values are for magnetic fields at the center of the cage of $\{0, 0, 0\}$ G and $\{-2, 1.5, -2\}$ G in the X, Y, and Z axes respectively with an ambient magnetic field of approximately 230 mG, -105 mG, and 433 mG. The estimated generated magnetic field represents the field generated as per Eq. (2.4) if the actual applied current is utilized in calculations.

Table 4.3: Actual Magnetic Field vs. Expected Magnetic Field

Coil	Actual Applied Current (A)	Estimated Generated Magnetic Field (mG)	Actual Generated Magnetic Field (mG)	Magnetic Field Percent Error (%)
X (85")	0.55	-224.2	-230.7	2.83
Y (88")	0.26	102.4	105.5	2.98
Z (91")	1.29	-415.0	-433.2	4.21
X (85")	5.62	-2290.65	-2230.7	2.69
Y (88")	3.96	1559.03	1611.9	3.28
Z (91")	6.23	-2371.86	-2433.2	2.52

As shown in Table 4.3 the error between the estimated magnetic field as calculated via Eqn. (2.4) and actual magnetic field generated varies from 2.52% to 4.21%. Several factors weigh into the error. First, the current was read from the digital display on the power supplies which only displays two significant figures after the decimal. When the current is controlled via GPIB, there are actually four significant figures after the decimal so the applied current can be slightly different than that on the digital display which affects estimated generated magnetic field calculations. Secondly, Eq. (2.4) is based upon square coils. Wire does not lend itself to square corners so some error will come from the fact that the corners are rounded. Also the wire bows out slightly at the mid-point of the coils making the shape slightly circular. Another possibility for the discrepancy between the actual and estimated values could be the power supplies not being calibrated at the time of testing. The last calibration

date for the Y axis control power supply was in 2005 and the other power supplies do not have a listed calibration date. The estimated resistance and applied voltage do not have an affect on the estimated magnetic field as Eqn. (2.4) does not depend on the resistance or voltage. The equation depends only upon the applied current, number of wrappings, and the spacing between the pair of coils. The actual values for the current, number of wrappings, and spacing were used in calculating the estimated values.

4.2.2 Zeroing the Ambient Magnetic Field. The next test performed with the Helmholtz cage tested the ability of the cage to zero the magnetic field across a test plane. The truth magnetometer was used to survey the magnetic field across the support platform within the cage with the center point commanded to have a 0 mG magnetic field in all 3 directions. Test setup was described in Sec. 3.5.4. The magnetic field vectors provided in Fig. 4.3 are scaled to one tenth of their original size to enable a clearer idea of the magnetic field across the test plane. The vectors are also in mG and therefore relatively small, but due to the required scaling of the axis the vectors appear large. The cage was zeroed around the point 0.75", 0", 0" in the X, Y, and Z directions, respectively, on the test plane as the test points were arranged slightly offset from the 0", 0", 0" point in the X, Y, and Z directions, respectively.

As shown in Fig. 4.3, the magnetic field in the back right corner of the cage and to the right of Fig. 4.3 had the largest magnitude with a vector of $\{41.5, -2.1, -2.21\}$ mG in the X, Y, and Z directions, respectively. This corner is in the -X and -Y direction near the corner of the room where a support column projects out from the wall approximately 6 inches in both directions. The column has a ferromagnetic material, likely rebar, which is likely affecting the magnetic field. The cage would have to be moved further from the corner to verify this theory. A computer and steel desk in the front right corner, or +X, -Y direction likely affected the magnetic field in this corner.

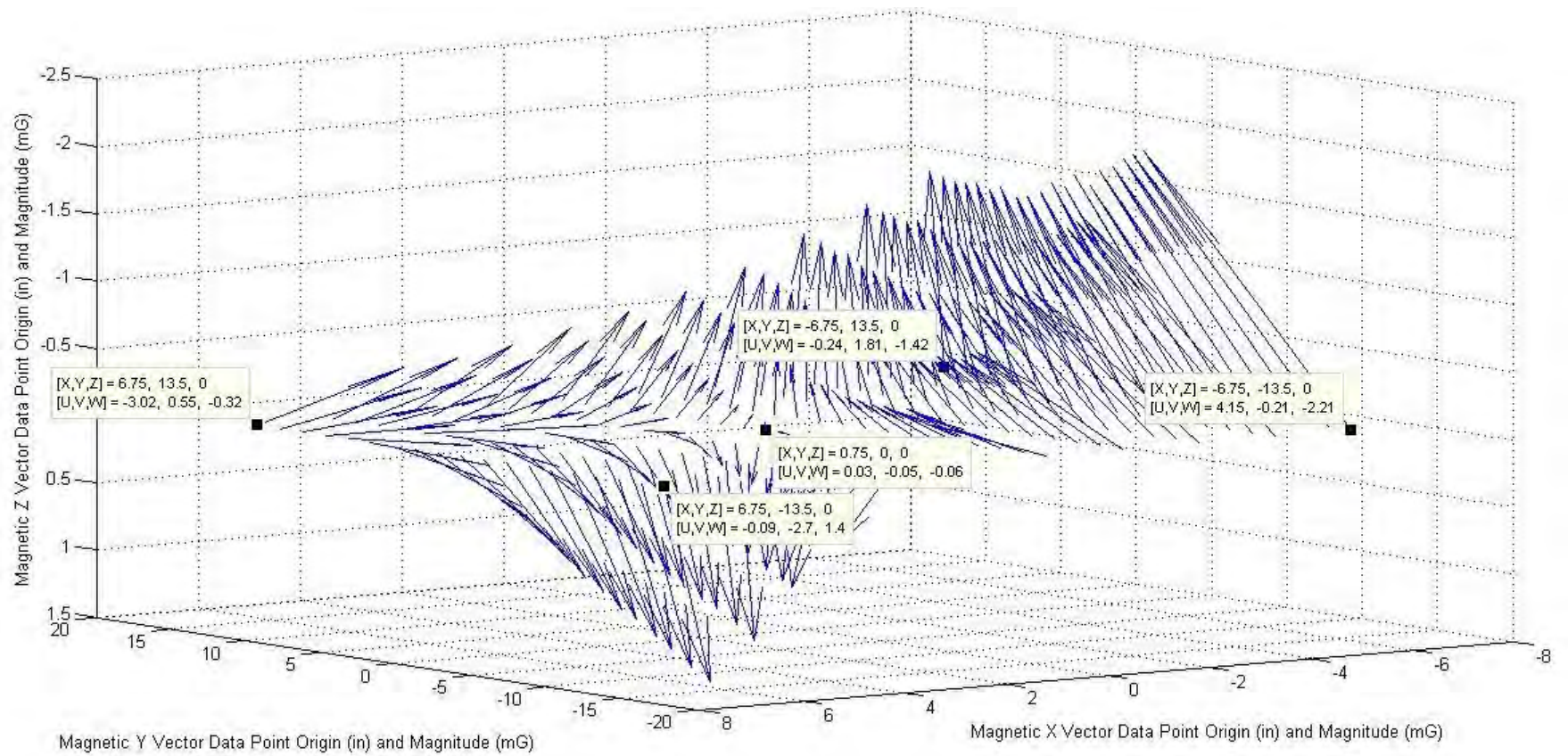


Figure 4.3: Magnetic Variance with Zeroed Cage Center (Vectors Scaled to $1/10^{th}$ Size - Cage Center at 0, 0, 0 mG)

It has been shown that the steel desk has a far reaching effect on the magnetic field so replacing the desk with the planned non-ferromagnetic desk should have a large impact. The magnetic field would have to be mapped again after the new, all aluminum desk is built. It is not a requirement to move the cage and install the desk as the magnetic field could be characterized for a commanded magnetic field so that if the magnetic field in one location is known from a truth magnetometer, the magnetic field at any other location on the test plane or even within a test volume is known. However it is very easy to move the desk and would make characterizing the field much easier.

It can be seen from Fig. 4.4 on the next page that the zeroed magnetic field vectors in blue follow the vertical displacement pattern of the ambient magnetic field highlighted in red. The zeroed magnetic field vectors have been scaled to one tenth of the original size and the ambient magnetic field vectors have been scaled to less than one thirtieth of the original size. The magnetic field as a whole has an angled appearance which would change with the increase in generated magnetic field in any direction. The ambient magnetic fields display the possible effects of the steel desk and reinforced column at the corners of the cage. The angles of the zeroed field vectors with respect to the test plane are much higher than the ambient fields thus the magnetic field generated by the cage amplified the effects of the desk and reinforced column. Again, these effects could be calibrated out for a known applied magnetic field.

Also of interest is a top view of the magnetic vectors across the test plane. Fig. 4.5 follows Fig. 4.4 and displays a top view of both the scaled ambient magnetic field in red and the zeroed cage center magnetic field in blue. To the right of the figure and therefore close to the wall with the support column in one corner and the desk in another the ambient field vectors had a larger magnitude than those to the left in the +Y direction. This is also evident in the zeroed magnetic vectors.

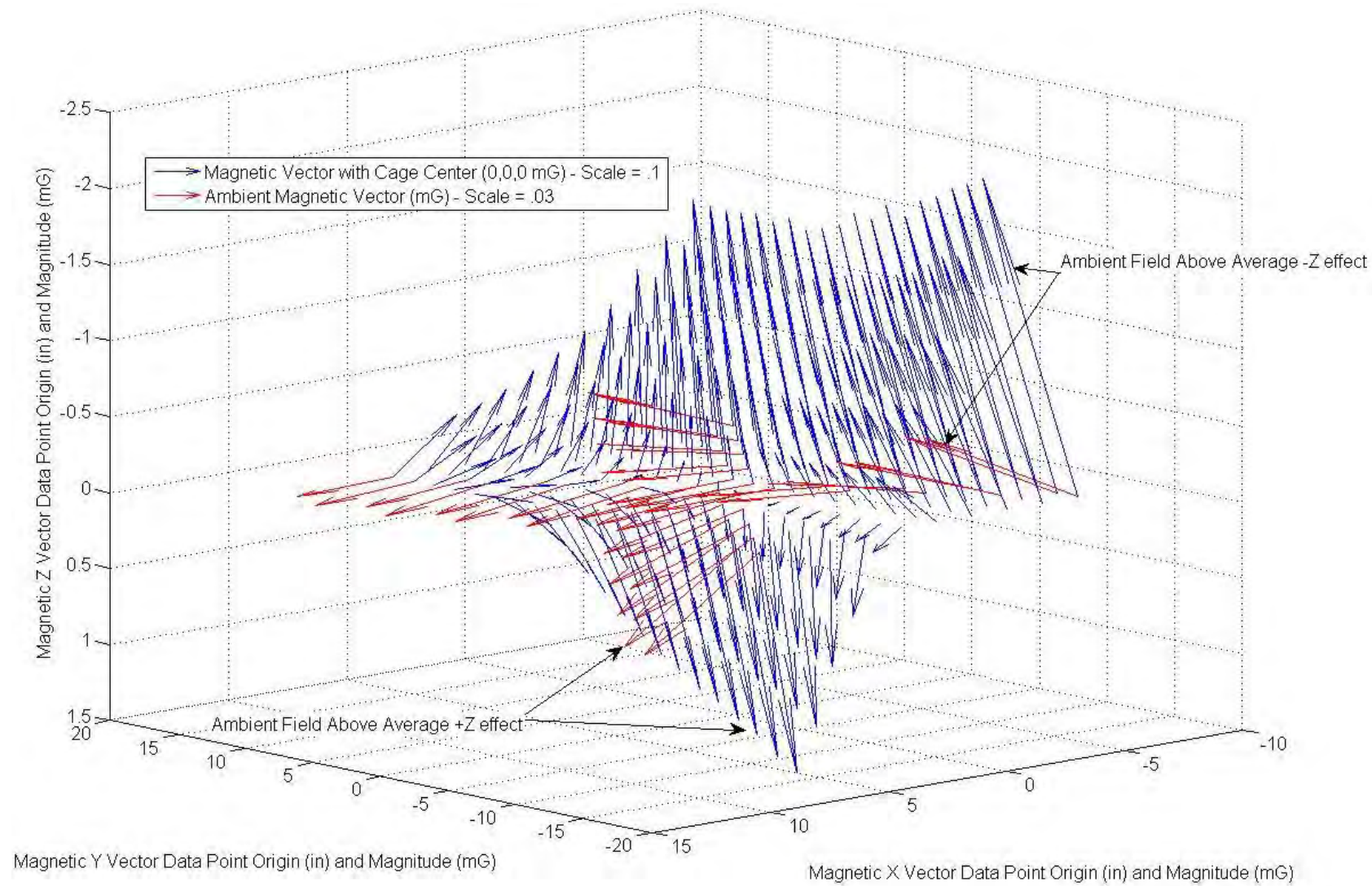


Figure 4.4: Ambient Field vs. Zeroed Field

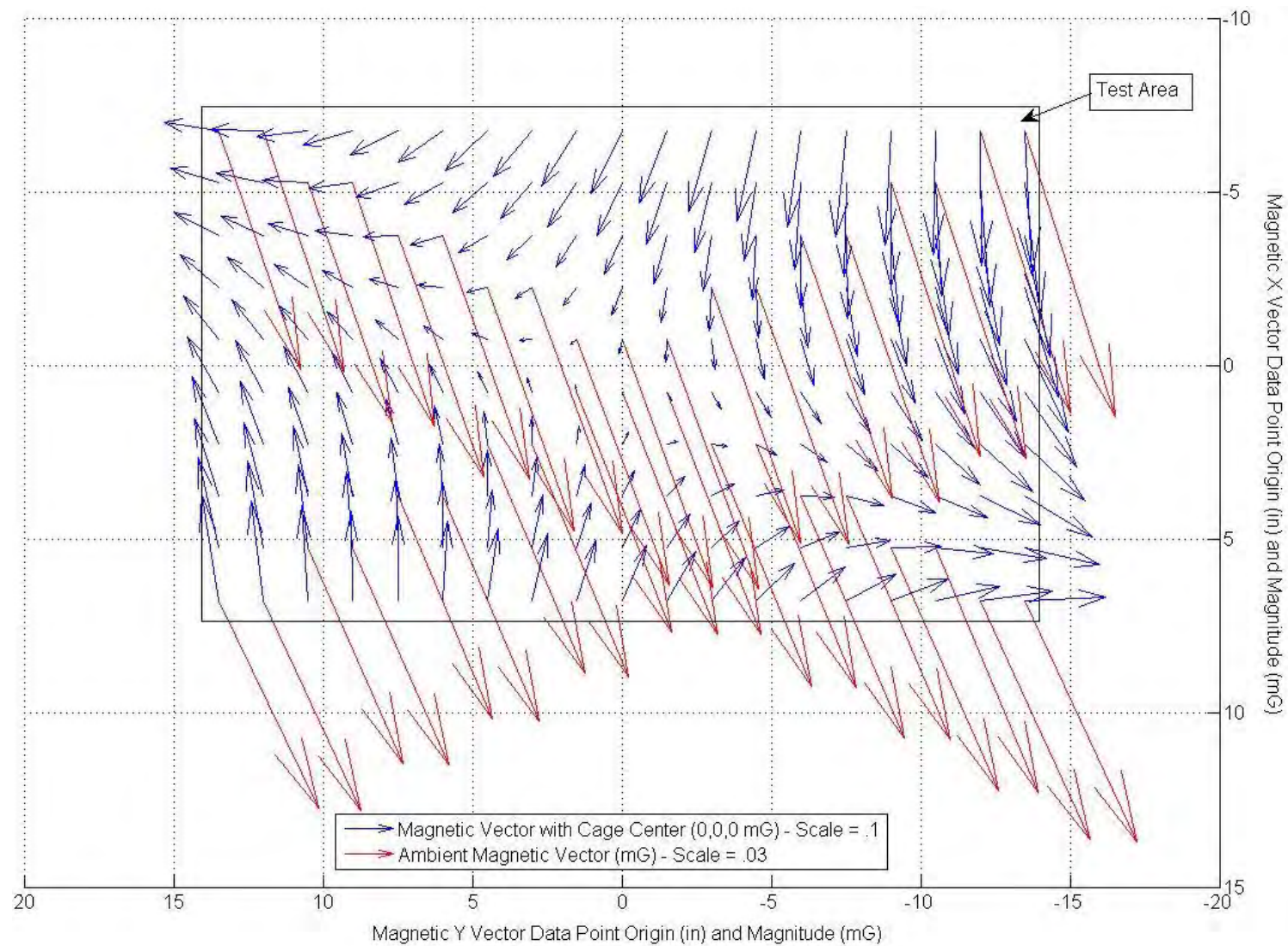


Figure 4.5: Top View of Ambient Field vs. Zeroed Field

The variation of the individual magnetic field components is displayed in Figs. 4.6 to 4.8. The support column in the back right or -X/-Y direction of the cage likely impacted the X component of the magnetic field. The steel desk in the +X/-Y direction likely was what impacted the Z and Y components of the magnetic field.

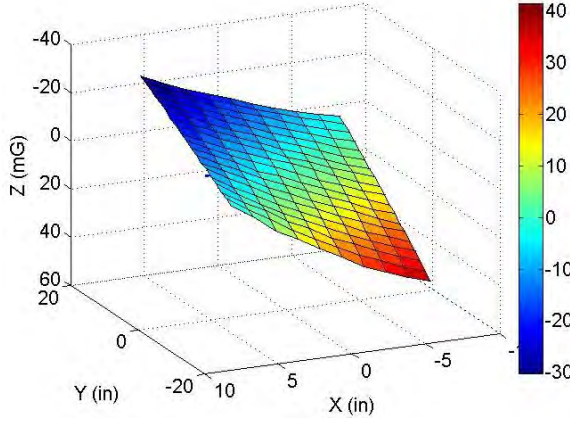


Figure 4.6: Variation of B_x - Cage Center at 0, 0, 0 mG

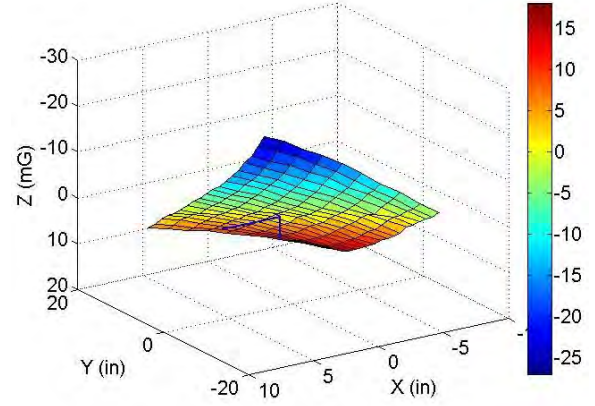


Figure 4.7: Variation of B_y - Cage Center at 0, 0, 0 mG

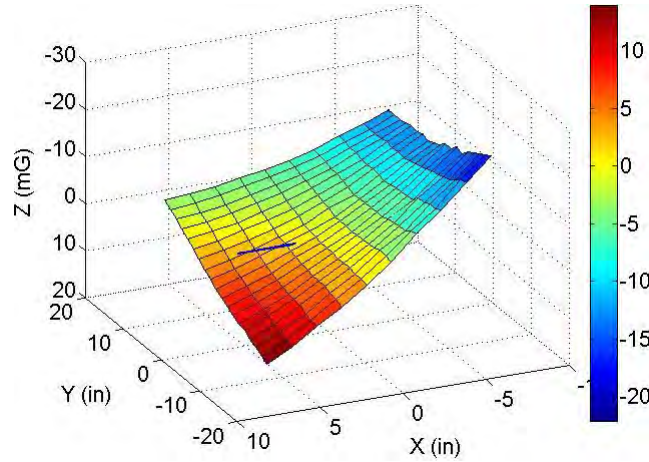


Figure 4.8: Variation of B_z - Cage Center at 0, 0, 0 mG

As expected, the cage was not able to completely zero the magnetic field uniformly across the test plane. At worst, the cage was able to change the ambient magnetic field from 273.3 mG X, -100.7 mG Y, and 402.5 Y mG in the back right corner of the cage to 41.5, -2.1, and -2.21 mG, respectively changing the length of the magnetic vector to one tenth the original length. Moving the cage away from the support column and replacing the desk with the planned non-ferromagnetic desk would

move the ambient magnetic field to a more uniform field, and it would ensure that the cage's magnetic field wasn't modified by these sources of error. A uniformity test would have to be reconducted to recharacterize the ambient field. Another option is to characterize the magnetic field for any possible generated magnetic field where an object such as a CubeSat or torque coil is going to be tested, preferably at the center where the cage is most uniform, and at the same time characterize a slightly offset location where the truth magnetometer would be during testing. By characterizing both locations, users would have knowledge of what the magnetic field at the test location is based on data from the truth magnetometer.

Removing the desk and moving the cage away from the support column in this scenario would likely increase the field of uniformity and therefore the test area. However, CubeSats, torque coils, and magnetometers are small objects that would typically be placed in the center of the cage where variations in homogeneity are small and therefore the deviations should not have a large affect on testing. Overall the deviations in the X direction are within 5% of the commanded X field within a 4" radius from the center of the cage, deviations in the Y direction are within 6%, and deviations in the Z direction are within 2%. NPS reported deviations of 2%, 6%, and 6% in the X, Y, and Z directions, respectively within a 3.825" radius. MEDA Inc. reports magnetic fields within 0.03% of the commanded field within an approximately 4" radius but this is when their cage is place far from ferromagnetic objects as discussed in Sec. 2.4. MEDA Inc. also uses a second set of coils for each axis to control the gradient of the magnetic field. TU Delft reported that reinforced concrete in the lab area causes the magnetic field to vary as much as 30 mG as discussed in Sec. 2.4. This is similar to the 41.5, -2.1, and -2.21 mG magnetic vector in the back right corner of the AFIT Helmholtz cage test plane caused by the support column in the corner of the room.

4.2.3 Dynamic Cage Control with STK. The results of the cage control test utilizing a magnetic field report generated in STK and commanded through MATLAB

are provided in Fig. 4.9. The “actual” data represents data recorded by the truth magnetometer for the magnetic field in the center of the Helmholtz cage and the “desired” data represents the magnetic field that a satellite in a 300 km altitude, 28° inclination orbit would experience in approximately 1.5 orbits. The profiles are similar and any differences are likely just a function of tolerances used in the ‘while’ loops within the MATLAB command script. For the dynamic control case shown in Fig. 4.9 the actual and desired magnetic field components are within ± 3 mG, ± 9 mG, and ± 8 mG in the X, Y, and Z directions with error standard deviations of 1.4, 1.6, and 1.1 mG in the X, Y, and Z directions, respectively.

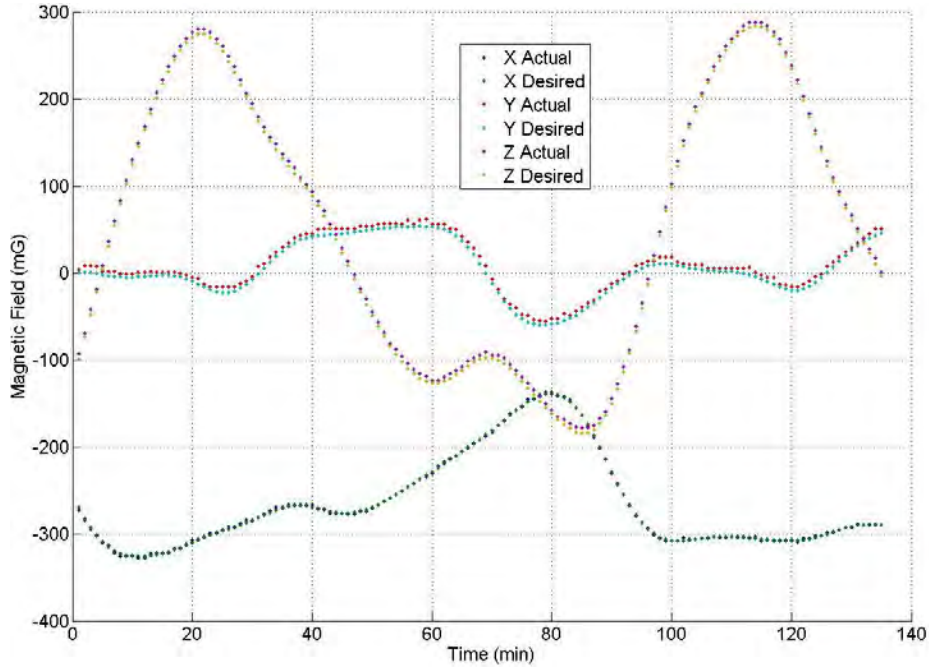


Figure 4.9: Generated Magnetic Field vs. Commanded

The desired values represent the magnetic field that a satellite would experience in one minute intervals. The actual data represents data that was collected once the script had obtained the desired magnetic field within certain tolerances. Sometimes the desired field was achieved within 5 seconds and sometimes it was achieved in 30 seconds, so the magnetic field in the cage currently does not change at one minute intervals. However, further development of the closed-loop control would enable a

consistent time interval between each step or perhaps ensure that the correct current was applied each time so the cage would achieve the desired time step.

4.3 On-board Magnetometer Analysis

4.3.1 Magnetometer Linearity. The linearity of the on-board magnetometer was tested by placing the truth magnetometer directly over the on-board magnetometer. The truth magnetometer was oriented with the cage reference frame while the CubeSat and the cage shared the same positive X direction and opposite Y and Z directions. The magnetic field as reported by the truth magnetometer was increased at 100 mG intervals in the Y direction from 0 to 1500 mG while holding the X and Z components at 0 mG. The X and Z components reported by the truth magnetometer increased with each interval by approximately 1 mG displaying the effect of one pair of coils on the other two coil pairs. Before data was collected from the on-board sensor the X and Y components were readjusted to 0 mG such that each set of test data was recorded only when the X and Z components were zero. The results of the test are displayed in Fig. 4.10 and Fig. 4.11.

The Y component of the magnetic field as shown in Fig. 4.10 is reported by the on-board magnetometer and is approximately linear; however, there is an associated gain as the on-board data grows at a faster rate than the actual magnetic field from the truth magnetometer. There is also an offset as the on-board magnetometer reported a value of 33 mG when the truth magnetometer reported a value of 0 mG. The gain for the Y component of the magnetic field is approximately 1.26 and the offset is 33 mG. Online forums for the on-board magnetometer suggested that a gain factor was important to obtain precision data from the magnetometer when utilizing it in a standard geomagnetic field on the surface of the Earth [51]. A gain factor was not utilized in the attitude determination algorithm, as discussed later in this chapter, but it may prove useful to increase the accuracy of the CubeSat's attitude determination capabilities. A separate gain for each axis may be required.

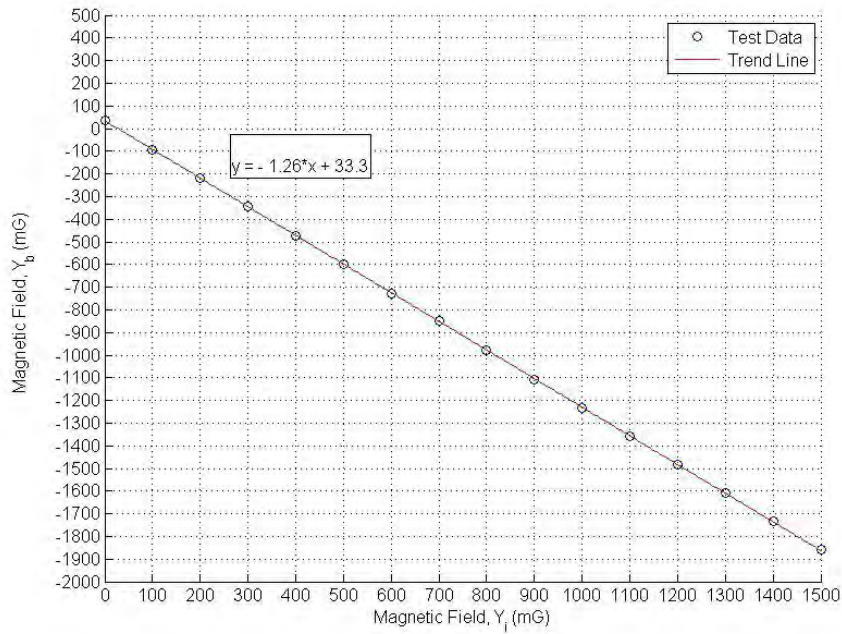


Figure 4.10: Linearity of Magnetometer in Y

The X and Z magnetic field data from the on-board magnetometer was also recorded during the same test. As previously mentioned, the X and Z components according to the truth magnetometer were set to 0 mG for each data set. The results are displayed in Fig. 4.11.

The magnetic field measured by the on-board magnetometer in the Z direction as shown in Fig. 4.11 stayed fairly consistent at 20 mG which is the offset of the magnetometer for the given magnetic field in the Y direction. The magnitude of the magnetic field in the X direction increased with an increase in magnetic field in the Y direction. The higher magnetic fields could be inducing a magnetic field across the circuitry of the 9 DOF or the on-board magnetometer and truth magnetometer may not be perfectly orthogonal. A difference of 30 mG in the on-board magnetometer X direction based on an increase in the truth Y magnitude of 1500 mG was not considered a big issue as 30 mG represents only 2% of the applied field.

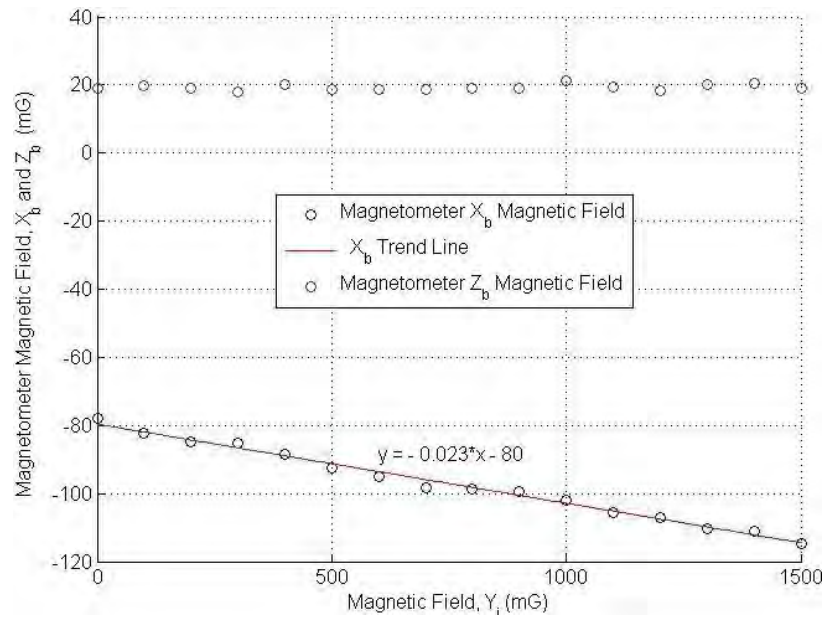


Figure 4.11: Linearity of Magnetometer in X and Z

4.3.2 Reaction Wheel Effects on On-board Magnetometer. The reaction wheels on-board the CubeSat have no apparent effect on the magnetometer as shown in Fig. 4.12. During testing the on-board magnetometer was located at the top of the CubeSat and not on the C&DH board.

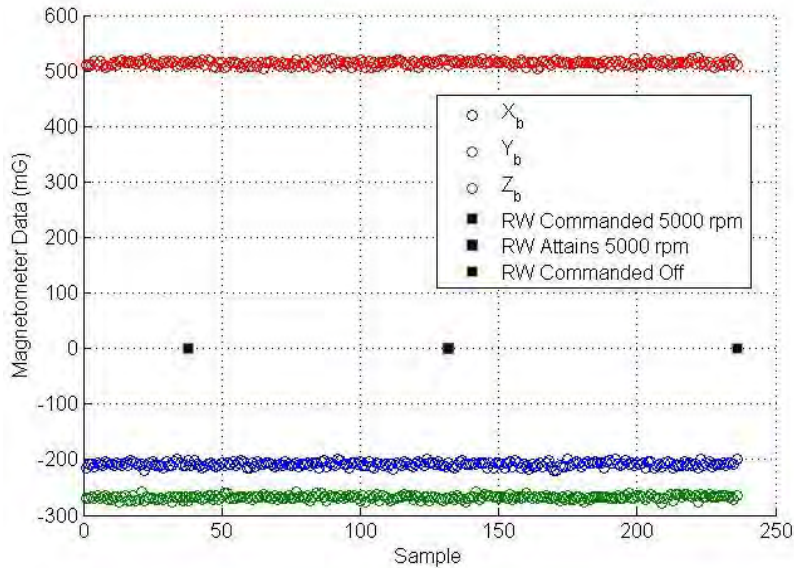


Figure 4.12: X Axis Reaction Wheel Effects on Magnetometer

The on-board magnetometer output was recorded as the reaction wheel correlating to rotation about the X-axis was commanded to 5000 rpm. Markers on Fig. 4.12 represent the data sample at which the wheel was commanded to a speed, when the wheel reaches that speed according to the command code, and when the wheel was commanded off. The magnetometer is not affected by the X-axis reaction wheel as it is cycled through an operation. Testing with the Z and Y axis wheels had similar results with no apparent effect on the on-board magnetometer. Later testing proved that the reaction wheels impact the magnetic field within approximately 2”.

4.3.3 Magnetometer Offset. Offset testing of a magnetometer is performed by rotating the magnetometer about each axis. The results per axis should be a circular mapping of the magnetic field centered around zero. The X and Z on-board magnetometer offset was tested for inertial magnetic components of $\{0, 0, -1\}$ G and $\{0, 1.5, 0\}$ G in X, Y, and Z respectively as recorded by the truth magnetometer when it was placed directly over the CubeSat on-board magnetometer. The CubeSat was oriented such that the +Z body axis was in the -Z inertial direction. The truth magnetometer was removed just before rotating the CubeSat about the Z body axis in both scenarios.

Testing with the magnetic field in the -Z direction of the cage showed that the magnitude in the Z direction of the on-board magnetometer would jump from 1576 to 4096 mG in the high magnetic field environment of -1.5 G in the inertial Z axis. For the first offset test this value was reduced to -1G to prevent possible discontinuities in the X and Y magnetic components as calculated by the on-board magnetometer. The on-board magnetometer magnetic field components were recorded and mapped in Fig. 4.13.

The resulting ellipse is centered at approximately 26 mG in the Y direction and -50 mG in X providing the offset values. The ellipse is also roughly circular so no gains would be necessary for achieving a circular mapping.

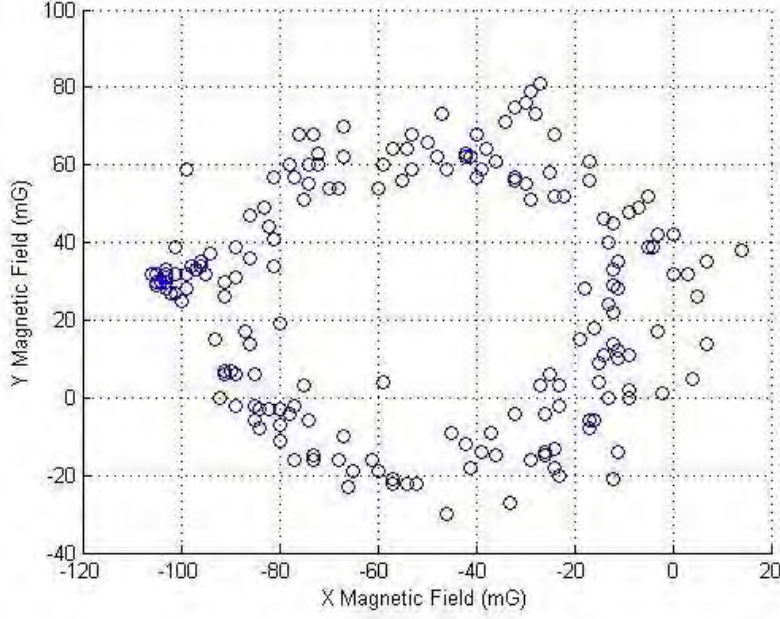


Figure 4.13: On-Board Magnetometer Offset with $B_{zi} = -1$ G

In the second offset test, the magnetic field of the cage was set to 1.5 G as per the truth magnetometer in the positive Y inertial direction to test the offset of the on-board magnetometer in the 1.5 G environment as attitude determination testing would utilize this value for testing. The CubeSat was placed in a $\{0, 1.5, 0\}$ G environment for the cage X, Y, Z directions, respectively. Results of rotating the CubeSat around its Z-axis in this environment are provided in Fig. 4.14.

The on-board magnetometer experienced a similar discontinuity in the X direction to that experienced in the Z direction when testing with an Z_i magnetic field. No discontinuities occurred in the Y direction. Note that the magnetometer is rated for ± 4 G according to the spec sheet [24]. Ignoring the discontinuities the resulting ellipse is centered around approximately 43 mG in the Y direction and approximately -70 mG in the X direction. The ellipse is roughly circular. The offset of this scenario differs slightly from the offset of the first scenarios indicating that the offset is a function of magnetic field direction and magnitude. Based on this information, the most accurate data from the magnetometer would be achieved by calculating the offset

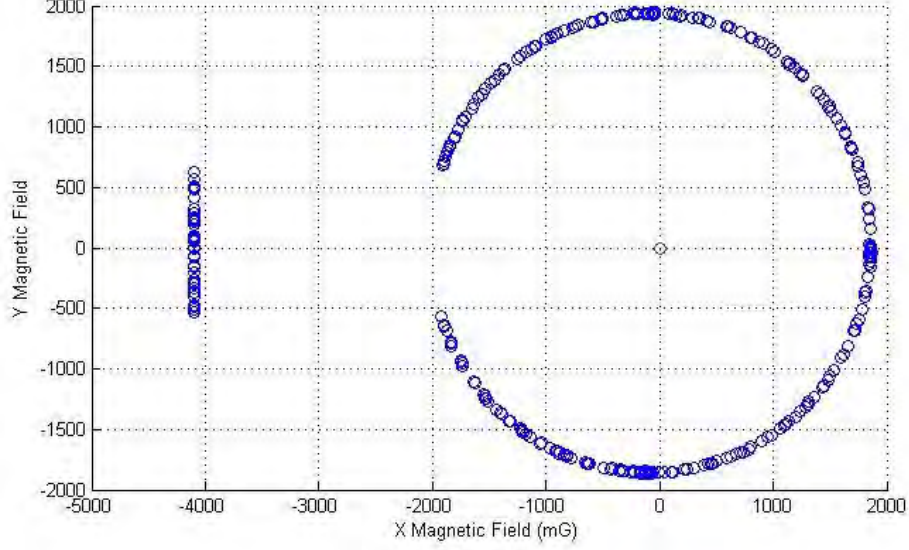


Figure 4.14: On-board Magnetometer Offset in 1.5 G Y_i Environment

for each possible inertial magnetic field vector and applying the appropriate gain as discussed in Sec. 4.3.1.

4.4 *CubeSat Attitude Determination*

4.4.1 OFQEA Testing with Magnetic Field in $-Z_i$. The optimal fast quaternion estimation algorithm (OFQEA) [16] was first tested by placing flashlights in the $\{1, 0, 0\}_i$ direction illuminating towards the center of the cage and the cage generating a magnetic field of $\{0, 0, -2\}_i$ G. The truth magnetometer was attached directly over the CubeSat to record the initial inertial magnetic field properties and then removed for testing. The CubeSat was rotated by hand on a compass rose in a counter clockwise direction about the CubeSat +Z axis and the Cage -Z axis as shown in Fig. 3.14 and discussed in Sec. 3.7. Accuracy of the by hand rotation was well within $\pm 1^\circ$ and therefore serves as the truth rotation. Further setup for this test is described in Sec. 3.7. The yaw or '3' Euler angle representation from a 1-2-3 rotation as calculated on-board the CubeSat from the quaternions of the OFQEA also calculated on-board the CubeSat are shown in Fig. 4.15. The maximum error in this testing was 19° .

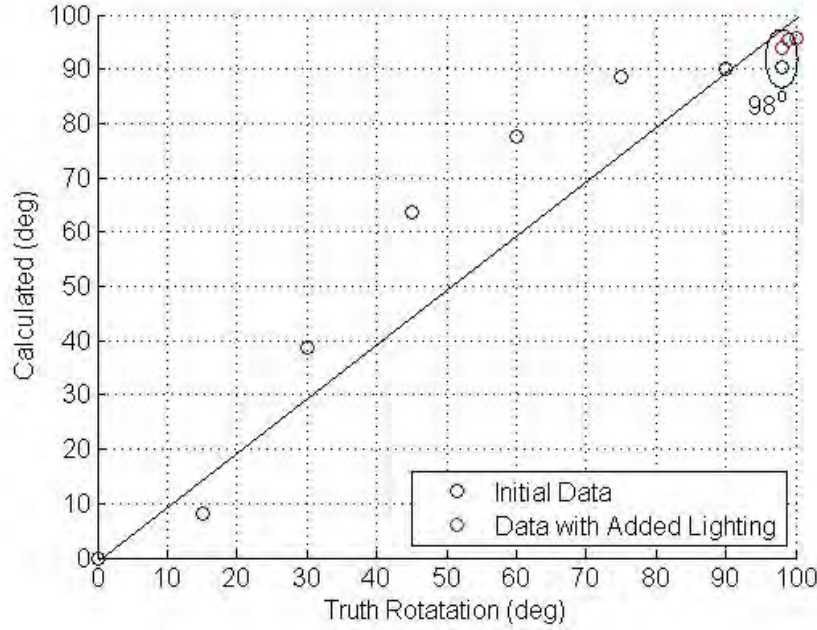


Figure 4.15: Yaw about Z_b with Magnetic Field $\{0, 0, -2\}_i$ G

Telemetry from the CubeSat demonstrated that the yaw angle about the Z_b axis matched the Sun azimuth calculations and that the magnetometer therefore had little effect on the yaw calculation in this configuration, hence Fig. 4.15 also represents the azimuth angle calculated from Sun sensor data for a rotation about Z_b with the Sun vector in the $\{1, 0, 0\}_i$. Sun sensor readings were low registering 10 units when a sensor was directly facing the lights out of a possible 1000+ units. Extra flashlights were added for higher rotation angles starting with 98° , however the sensor reading only improved to 14 units. Data points highlighted in red in Fig. 4.15 represent data with more flashlights. Two data points exist at 98° one with the added flashlights and one without. The error at this point decreased from 8° to 4° with the addition of flashlights. Error would likely decrease for all angle calculations with the addition of more light. However, it is possible with an increase in light that the light could reflect off the side of the cage opposite the flashlights or even the paint on the wall which could theoretically increase the error. Fortunately, the algorithm currently utilizes the maximum value of the two sensors on an axis which negates the issue of reflected light.

4.4.2 *OFQEA Testing with Magnetic Field in Y_i .* The OFQEA was tested again by placing flashlights in the $\{1, 0, 0\}_i$ direction and generating a magnetic field of $\{0, 1.5, 0\}_i$ G. Additional flashlights were added on top of those mentioned in the previous test so that maximum Sun sensor values were at 25 units. Results are shown in Fig. 4.16.

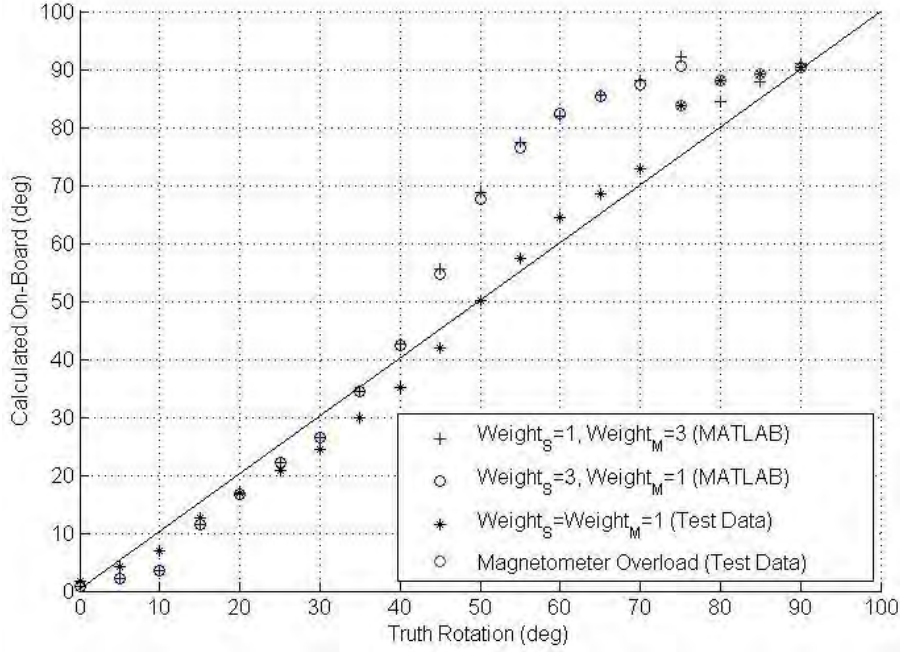


Figure 4.16: Yaw Accuracy

Fig. 4.16 displays the actual test data where the on-board Sun sensors and magnetometer have equal weights $Weight_S$ and $Weight_M$, respectively, as part of Eqn. 2.21. During the latter portion of the test, the magnetometer values jumped to 4096, or saturation, changing the on-board calculated magnetic field in the body frame affecting the body magnetic unit vector used for calculations. The affected angles are represented by red circles. Effectively the Y and Z components contributed less to the body magnetic unit vector affecting the accuracy of the Euler angles. This could be changed by reducing the inertial magnetic field to 1.2 G or lower based on data from Figs. 4.14 and 4.10. MATLAB code was later generated that matched the test data exactly and then modified for different weights for the Sun sensor and

magnetometer of 1 and 3 and then vice versa. This data was also plotted in Fig. 4.16. Equally weighting of 1 for the two sensors provided the greatest accuracy.

The error between the actual rotation about the body Z axis and the rotation calculated by the CubeSat are provided in Table 4.4.

Table 4.4: Accuracy of OFQEA

Truth Angle (Degrees)	Error (Degrees)
0	1.7
5	-0.76
10	-3.10
15	-2.27
20	-3.15
25	-4.29
30	-5.55
35	-5.01
40	-4.88
45	-3.09
50	0.21
55	2.47
60	4.37
65	3.57
70	2.82
75	8.73
80	8.11
85	4.30
90	0.35

Worst case, the error was less than 6° except for the cases of 75° and 80° . However, these larger errors occurred when the on-board magnetometer experienced the discontinuity in the X component. Discontinuities also occurred at 85° and 90° however these angles would be less effected by the discontinuity as the magnetic field body vector Y and Z components for this rotation are small in magnitude and therefore have less of an impact on attitude determination. Effectively, this unit vector in the body frame would be roughly $\{0, 0, -1\}$ and it does not matter if the full vector was $\{0, 0, -4096\}$ or $\{0, 0, -1800\}$. With the data as is the average error was 3.62° . Theoretically, the mean and maximum error from 0° to 45° should equal the mean and maximum error from 45° and 90° as the CubeSat has rotational symmetry about

the Z_b axis . By using the values from 0° to 45° a maximum error of 5.55° and mean error of 3.38° is achieved.

If the CubeSat relied solely on the Sun sensors for attitude determination during this test the resulting roll angle would have been the opposite direction but same magnitude as the angles shown in Fig. 4.17.

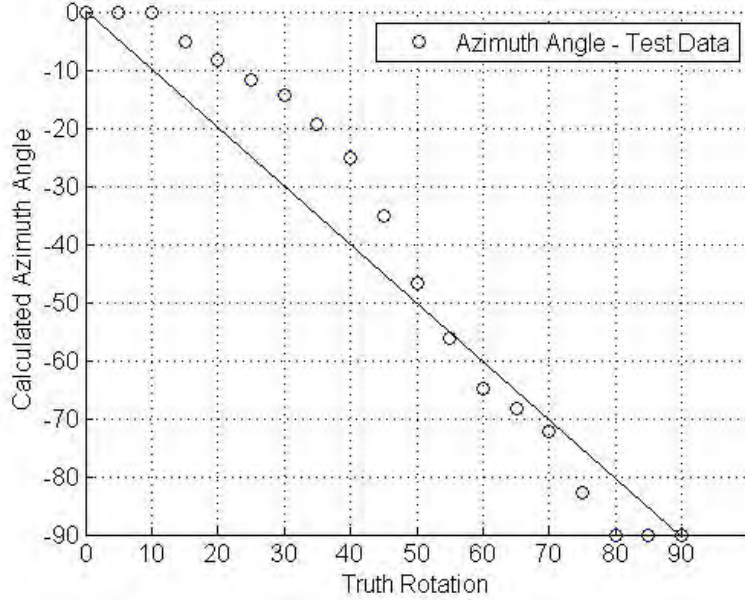


Figure 4.17: Sun Azimuth Angle

The Sun azimuth angles represent the horizontal angle from the X_b axis to the Sun vector. The flashlights were at the same level as the Sun sensors thus the elevation angle is 0° . The overall accuracy of the Sun sensors did improve with added flashlights as compared to the accuracy as depicted in Fig. 4.15; however, the addition of the on-board magnetometer OFQEA algorithm greatly improved the accuracy by reducing the error from 15° as shown in Fig. 4.17 to 6° as shown previously in Fig. 4.16.

Similar to the yaw error, roll and pitch error increased when the weights were not equal. The roll angle in the 1-2-3 rotation sequence was effectively 0° and the truth pitch angle was approximately -180° . Roll corresponds to the CubeSat rotating around the Y_b axis and the error in this test was within tenths of a degree. For

many CubeSat applications, this tenths of a degree is a very acceptable error. On-board magnetometer offsets were probably a cause of error in this scenario. Also the truth magnetometer and on-board magnetometer may not have been perfectly aligned. Pitch corresponds to the CubeSat rotating about the Z_b axis and the error was within three degrees. Error is again from the on-board magnetometer offset and possible misalignment. The stand was leveled as best as possible but some error likely comes from a tilt of the stand.

4.4.3 Optimal Method vs. TRIAD. As mentioned in Chapter 2, OFQEA results have only been simulated and compared to simulated results of the TRIAD algorithm in [16]. It was demonstrated in the simulations that the TRIAD estimate was almost as accurate as the optimal estimate. In this thesis, the OFQEA was implemented on the CubeSat and actual test data with estimated Euler angles was produced as demonstrated in Sec. 4.4. The raw data from the on-board magnetometer and the Sun sensors was also used in post processing to compute the TRIAD Euler angles via MATLAB. The yaw Euler angle representations of both the OFQEA CubeSat test and the TRIAD MATLAB simulation is provided in Fig. 4.18.

As confirmed in Fig. 4.18, in a hardware demonstration the OFQEA is more accurate than the TRIAD method as demonstrated in MATLAB simulations, which is to be expected because OFQEA is an optimized algorithm. In [16], it was noted that there were “marginal gains” in accuracy over the TRIAD method; however, in this test scenario the TRIAD method had yaw errors up to 15° when the OFQEA has yaw errors no greater than 6° not including the 75° to 90° when the on-board magnetometer incurred a discontinuity. Pitch error was similar for both algorithms with the truth pitch angle of -180° , but the rotation angle was not varied over a wide span of angles. A separate test with a larger variation of the angle would likely confirm that the OFQEA is more accurate than TRIAD. The TRIAD roll error was more accurate than the OFQEA with a truth rotation of 0° but the errors are within tenths of a degree of each other. The OFQEA was coded in the Arduino language

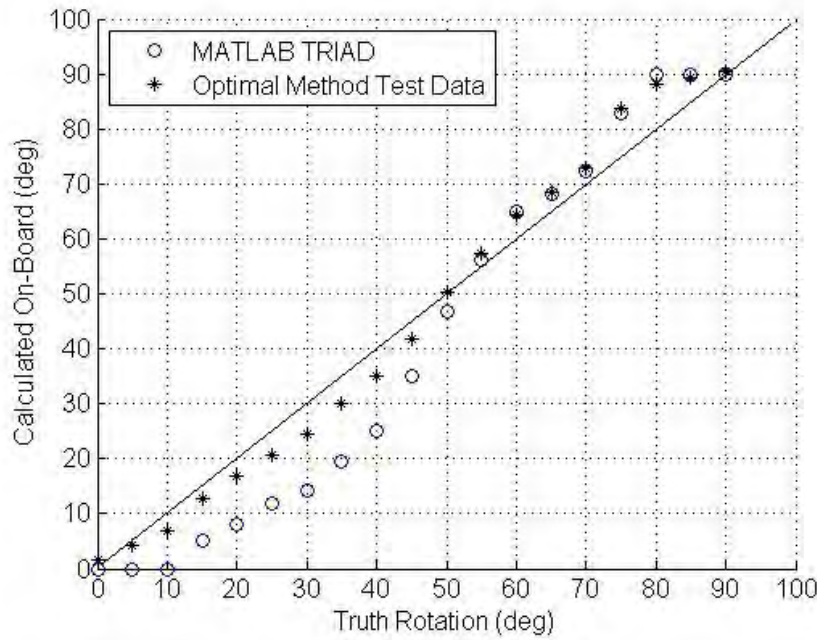


Figure 4.18: Optimal Method vs. TRIAD - Yaw

using user written cross product, normalization, and dot product functions along with matrix math written in long form. It's possible that some significant factors did not carry through in the code affecting the accuracy of the test data to within tenths of a degree whereas the MATLAB TRIAD code was written in 11 lines and utilizes MATLAB's built-in functions and ability to perform matrix multiplication hence the TRIAD roll angle of exactly 0° .

4.5 Summary

Chapter IV presented the results and analysis of performance tests. The magnetic field at the center of the cage is influenced by a steel desk at one corner of the cage and a support column at another corner. The cage is capable of achieving ± 2 G in the X and Z directions but is only capable of $+1.5$ and -1.7 G in the Y direction as a function of the power supplies utilized for the Y axis control. The cage is capable of simulating the on-orbit dynamic geomagnetic field within certain tolerances.

Testing of the on-board magnetometer showed that the magnetometer appears to saturate in the X and Z directions when the ambient magnetic field is above 1.2 G. Also it was shown that the magnetometer is not influenced by the reaction wheels when the on-board magnetometer is at the end of the CubeSat opposite of the reaction wheels. The optimal method was proven to provide yaw attitude determination within 6° with a Sun vector in the $+X_i$ direction and the magnetic vector in the $+Y_i$. Accuracy of the yaw attitude determination when the magnetic vector was in the $-Z_i$ was within 19° .

V. Conclusions and Recommendations for Future Development

5.1 Summary

This research was focused on building a Helmholtz cage to control the magnetic field at the center of the cage where an attitude control algorithm was tested on an engineering development unit (EDU) CubeSat. The selected algorithm has not been tested in satellite hardware before and is dependent upon a light source and the magnetic field generated by the cage. Chapter I provided the goals of this research including the goal to build a Helmholtz cage to enable future testing of a CubeSat and implementing an attitude determination algorithm on-board a 3U CubeSat with a long-term goal of enabling AFIT to build a CubeSat for launch. These goals were met in this research effort.

Chapter II provided the background on CubeSats, attitude sensors, the geomagnetic field, Helmholtz coils and cages, and several attitude determination algorithms. Chapter III builds upon the information provided in Chapter II to design and build the AFIT Helmholtz cage. Also, a description of the MATLAB dynamic cage control script is provided in Chapter III as is a description of how the cage was tested. Chapter III also includes a description of the Sun sensors and magnetometer on-board the CubeSat. The reasoning for selecting the optimal fast quaternion estimation algorithm (OFQEA) is discussed in Chapter III as is the methodology for testing OFQEA on-board the CubeSat.

Finally, Chapter IV provides the results and analysis of the cage and attitude determination tests. First, an analysis of the impact of ferromagnetic items in the classroom environment is analyzed followed by a survey of the geomagnetic field in the room pre-cage. The resultant magnetic field capability is provided as is a discussion on the ability of the cage to zero the geomagnetic field across the test plane. A support column in the corner of the room and a steel desk are affecting the uniformity of the field. The steel desk is to be replaced with an all aluminum desk and the cage can either be moved from the corner to minimize the effects of the support column, or the

magnetic field across the test plane can be characterized for a desired magnetic field. Also in Chapter IV is an analysis of the cage's ability to model the geomagnetic field on-orbit which showed that the cage is capable of achieving the desired magnetic field within certain tolerances.

Further analysis in Chapter IV showed that the on-board magnetometer is linear, but has an associated gain and offset as was demonstrated for the Y component of the on-board magnetometer data. The reaction wheels are shown to have no effect on the on-board magnetometer during any operation of the reactions wheels. The on-board magnetometer should not be placed within 2" of the reaction wheel assembly. An analysis of the performance of the OFQEA as tested in hardware is provided in Chapter IV along with an analysis of the effects of different weighting on sensors and a simulated comparison to the Tri-Axial Attitude Determination System (TRIAD) algorithm. The CubeSat is capable of determining its rotation about the longitudinal axis to within 6° when the Sun vector and magnetic vector are on the plane perpendicular to the axis of rotation. The 6° accuracy of the OFQEA attitude estimate in this scenario is shown to be better than the 15° accuracy of the TRIAD algorithm.

5.2 Conclusions

The AFIT Helmholtz cage is capable of achieving magnetic fields of ± 2 Gauss in the X (North) and Z (Vertical) directions in testing as desired. Greater magnetic fields are possible; however, the truth magnetometer does not measure above this value so there is no way of confirming the exact magnetic values above this measure. In the Y (East) direction the achievable magnetic field is only -1.692 G to 1.506 G as a function of the power supply utilized for this coil. If the power supply is replaced by the same power supplies as thosed used for the X and Z coils then the desired ± 2 G is fully achievable. The cage was successfully connected to STK and can easily simulate the geomagnetic field a satellite would experience on orbit.

The ambient magnetic field of the cage does have an effect on the homogeneity of the generated field. However, the homogeneity would improve by moving the cage further away from the corner which has a large concrete column with ferromagnetic material and by removing the steel desk nearby. The field could then be re-characterized such that knowledge of the magnetic vector in one location provides knowledge of the magnetic vector on the rest of the test plane.

Without the Helmholtz cage, it would be extremely difficult to verify that the on-board magnetometer outputs for the X, Y, and Z components of the magnetic field actually correspond to the X, Y, and Z directions. The on-board magnetometer is linear with respect to a linear increase in the magnetic field; however, there is an associated gain and a discontinuity that occurs in the X and Z components of the on-board magnetometer when its reading is above 1.5 G or when the truth magnetometer reads approximately 1.2 G or above. The discontinuity appears as saturation and so far only occurs with the X and Z outputs of the on-board magnetometer.

The magnetometer was moved from the C&DH card to the end of the CubeSat furthest from the bus as the C&DH card has a circuit that generates its own magnetic field when introduced to a high magnetic field generated by the cage. All of the other cards including the EPS and battery board as well as the reaction wheel assembly of the CubeSat were tested for induced magnetic fields in the high magnetic field environment and all had a negligible impact. It was also confirmed that the three reaction wheels do not have an effect on the on-board magnetometer when the magnetometer is at the end of the CubeSat.

With the flashlight aligned with the X axis and the magnetic field aligned with the Z axis the yaw accuracy achieved by the optimal fast quaternion estimation algorithm (OFQEA) as calculated by the CubeSat was within 19° as the attitude determination relied solely on the Sun sensors. When the flashlights and magnetic field were both on the X-Y plane, the OFQEA provided yaw estimates accurate to within 6° if the magnetometer was not saturated. A MATLAB simulation utilizing

the raw data from the test showed that equally weighting the Sun sensors and magnetometer provided better accuracy than weights of 1 and 3 for the Sun sensor and magnetometer respectively and vice versa. The raw data was also utilized to compare the accuracy of the TRIAD method as computed via MATLAB versus the OFQEA test data. TRIAD had significant errors up to 15° compared to the 6° error as per OFQEA. The most likely reason for the error is the fact that OFQEA is an optimized method which minimizes Wahba's cost function as defined in Chapter II. Based on the testing performed in this paper, OFQEA is an acceptable algorithm for calculating a spacecraft's attitude to within 6° if similar hardware is used.

5.3 Recommendations for Future Development

5.3.1 Finalizing the Cage. The permanent plastic coil supports should be installed to prevent conduction between the coils and the outer cage support and the permanent aluminum desk should be completed and installed so that there is a location for the laptop that controls the power supplies and reads data from the truth magnetometer. The desk should also include the rack for the power supplies as well as a spot for the switch relays. Replacing the Y coil power supply with a power supply similar to those used for the X and Z coils would permit a magnetic field in the Y direction of at least ± 2 G.

Once the relays are installed, the MATLAB dynamic cage control script for controlling the power supplies will need to be adjusted so that it commands the power supply that controls the switch relays. The control algorithm could be updated with tighter tolerances and improved closed-loop control to produce a desired magnetic field. The timing at which the cage achieves the desired magnetic field could be modified so that the produced magnetic field occurs at the time intervals provided in the STK geomagnetic field report. A graphical user interface (GUI) for the dynamic cage control script would be beneficial for the user by enabling the cage to be commanded graphically to a static magnetic field or to modify parameters of the geomagnetic field report from STK such as the time step or number of orbits the cage should simulate.

In order to produce a more uniform field over the entire test volume, the cage should be moved further away from the corner of the room as the support column is affecting the magnetic field in that corner of the cage; however this may not be possible due to space constraints in the classroom. The steel desk should also be removed to produce a more uniform field over the entire test volume. A completely uniform field is not necessary as objects tested in the cage will likely be within the small area of minimal variation at the center of the cage and as long as external influences on the ambient magnetic field are static the variation of the field can be accounted for in testing.

5.3.2 Attitude Determination. Any magnetometer used in future testing should be tested for discontinuities, gains, and offsets. If the same magnetometer is to be used, the magnetic field as calculated by the truth magnetometer should not exceed 1.2 G to prevent saturation. Adding more light to the Sun simulator may increase the accuracy of the attitude determination, but it is likely worthwhile to explore other sensors. For example, star sensors could be tested by adding LEDs to the cage as described in [52].

Future iterations of attitude determination via the test CubeSat could incorporate different algorithms including the optimized QUEST algorithm described in Sec. 2.6.2.2. Future research should also include Kalman filters. The gyroscopes on-board the 9 DOF could be used to update the attitude estimate between sensor collections should the CubeSat rotate at a rate high enough that the sample rate of the sensors does not provide an accurate enough estimate of attitude. Also, the inertial magnetic vector could be calculated on-board the CubeSat from time data from STK or perhaps with location data from STK representing an on-board GPS resulting in an inertial magnetic vector that is calculated on-board from IGRF tables. This would provide for a more dynamic attitude determination test.

A better truth rotation device than the compass rose could be installed to enable dynamic rotation analysis. A video camera is one possible method or a non-

ferromagnetic digital rotation sensor. Adding a non-ferromagnetic air bearing would also greatly aid in possible future 3-axis attitude determination or control testing. A short term solution providing rotation about one axis would be to suspend the test specimen from a non-ferromagnetic cable attached to the top of the cage.

5.4 Future Applications of the Helmholtz Cage

The Helmholtz cage could also be utilized to test not only space concepts but also concepts like geomagnetic navigation on a small scale, magnetoresistive materials [53], or magnetorheological fluids which respond to a magnetic field with an increase in viscosity [53]. From a space related standpoint, the Helmholtz cage provides AFIT the opportunity to further design, test, and evaluate satellite concepts. Not only can more attitude determination algorithms be tested with the Helmholtz cage, but different sensors can be tested in combination with the magnetometer. Torque coils as an attitude control method can also be tested. If the torque coils are designed to operate in the frictionless environment of space but do not work in testing due to air drag, the ambient magnetic field could be increased to overcome the drag. Magnetic issues such as the residual dipole of a satellite can be analyzed. Testing of magnetic payloads and magnetometer verification are just examples of other test applications of the AFIT Helmholtz cage. Other universities could utilize AFIT's cage for testing their torque coils, CubeSats, and magnetic payloads. The cage is *the solution* for testing and verifying a magnetic component of any AFIT CubeSat, whether that component is only for educational purposes or built for launch.

Bibliography

1. Nave, C., "Magnetic Field of the Earth," <http://hyperphysics.phy-astr.gsu.edu/hbase/magnetic/magearth.html>, 2011, [Online; Accessed 25-November-2011, Reprinted with permission from C.R. Nave. Copyright 2010].
2. NASA, "Earth's Inconsistent Magnetic Field," http://www.nasa.gov/vision/earth/lookingatearth/29dec_magneticfield.html, 2003, [Online; Accessed 25-November-2011].
3. NASA, "Heliophysics Laboratory," http://ccmc.gsfc.nasa.gov/support/HSS_2011.php, 2011, [Online; Accessed 30-November-2011].
4. Love, J., "Magnetic Monitoring of Earth and Space," http://geomag.usgs.gov/downloads/publications/pt_love0208.pdf, 2008, [Online; Accessed 4-Jan-2012].
5. Smith, D., "Helmholtz Coils," <http://physicsx.pr.erau.edu/HelmholtzCoils/index.html>, [Online; Accessed 21-December-2011, Reprinted with permission from D. Smith].
6. Rudd, M. and Craig, J., "Optimum Spacing of Square and Circular Coil Pairs," <http://digitalcommons.unl.edu/physicsrudd/41>, 1968, [Online; Accessed 9-Oct-2011; Reprinted with permission from Optimum Spacing of Square and Circular Coil Pairs. Copyright 1968, American Institute of Physics].
7. Lee, G., Kang, C., and Chang, J., "Square Loop Coil System for Balancing and Calibration of Second-Order SQUID Gradiometers, 2011 IEEE," *IEEE Transactions on Applied Superconductivity*, Vol. 17, No. 2, 2007, pp. 3769–3772.
8. MacIntyre Electronic Design Associates (MEDA), I., "HCS01CL With Gradient Coils Operation and Maintenance Manual," 2007.
9. Poppenk, F. and Amini, R., "Delfi-C3 Control System Development and Verification," *57th International Astronautical Congress*, 2006.
10. Klesh, A. et al., "Dynamically Driven Helmholtz Cage for Experimental Magnetic Attitude Determination," Pittsburgh, PA, 2009, March, Reprinted with permission from the author, Credited to the University of Michigan 2009.
11. Swenson, E., "Intermediate Spacecraft Dynamics - Part I," Mech 632 Lecture Notes, 2011.
12. Larson, W. and Wertz, J., *Space Mission Analysis and Design, Third Edition*, Microcosm Press and Springer, 2006.
13. Pisacane, V. and Moore, R., *Fundamentals of Space Systems*, Oxford University Press, 1994.
14. Wertz, J., *Spacecraft Attitude Determination and Control*, D. Reidel Publishing Company, 1978.

15. Lee, J. and Park, E., "Minimum-Order Kalman Filter With Vector Selector for Accurate Estimation of Human Body Orientation," *IEEE Transactions on Robotics*, Vol. 25, No. 5, 2009, pp. 1196–1201.
16. Markley, L., "Fast Quaternion Attitude Estimation from Two Vector Measurements," http://www.archive.org/details/nasa_techdoc_20010068636.
17. Schuster, M., "1981a," http://www.malcolmdshuster.com/comm_1981a_J_TRIAD-QUEST.pdf, [Online; Accessed 6-Jan-2012].
18. Hall, C., "Chapter 4 Attitude Determination," <http://www.dept.aoe.vt.edu/~cdhall/courses/aoe4140/>, 2003, [Online Lecture Notes; Accessed 6 Jan 2012].
19. Malik, T., "What's Shakin'? Tiny Satellite to Try and Predict Earthquakes," http://web.archive.org/web/20061110153210/http://www.space.com/businessstechnology/technology/quakesat_detection_030423.html, 2003, [Online; Accessed 16-November-2011].
20. NASA, "GeneSat-1," <http://www.nasa.gov/centers/ames/missions/2007/genesat1.html>, 2007, [Online; Accessed 16-November-2011].
21. Sellers, J. et al., *Understanding Space - An Introduction to Astronautics, Second Edition*, the McGraw-Hill Companies, Inc., 200.
22. InvenSense, I., "ITG-3200 Product Specification Revision 1.4," <http://www.sparkfun.com/datasheets/Sensors/Gyro/PS-ITG-3200-00-01.4.pdf>, 2010, [Online; Accessed 19-July-2011].
23. Apostolyuk, V., "Theory and Design of Micromechanical Vibratory Gyroscopes," <http://www.astrise.com/research/library/memsgyro.pdf>, 2006, [Online; Accessed 1-Nov-2011].
24. Honeywell, "3-Axis Digital Compass IC HMC5843," <http://www.sparkfun.com/datasheets/Sensors/Magneto/HMC5843.pdf>, 2009, [Online; Accessed 16-Nov-2011].
25. Bratland, T., e. a., "A New Perspective on Magnetic Field Sensing," <http://www.sensorsmag.com/sensors/electric-magnetic/a-new-perspective-magnetic-field-sensing-855>, 1998, [Online; Accessed 20-Dec-2011].
26. Pisacane, V., *The Space Environment and Its Effects on Space Systems*, American Institute of Aeronautics and Astronautics, 2008.
27. Glatzmaier, G., "The Geodynamo," <http://es.ucsc.edu/~glatz/geodynamo.html>, [Online; Accessed 25-November-2011].
28. Sandeman, K., Hopwood, C., and Brook, C., "Ferromagnetic Materials," <http://www.doitpoms.ac.uk/tlplib/ferromagnetic/printall.php>, 2008, [Online; Accessed 25-November-2011].

29. Nave, C., "Magnetic Properties of Solids," <http://hyperphysics.phy-astr.gsu.edu/hbase/solids/magpr.html#c1>, [Online; Accessed 25-November-2011; Reprinted with permission from C.R. Nave. Copyright 2010].
30. (HAARP), T. H. F. A. A. R. P., "About the Ionosphere," <http://www.haarp.alaska.edu/haarp/ion1.html>, [Online; Accessed 25-November-2011].
31. Survey, B. G., "The Earth's Magnetic Field: An Overview," <http://www.geomag.bgs.ac.uk/education/earthmag.html>, [Online; Accessed 4-Jan-2012].
32. Oceanic, N. and Administration, A., "Further Understanding of Geomagnetism," <http://www.ngdc.noaa.gov/geomag/geomaginfo.shtml>, [Online; Accessed 25-November-2011].
33. Incorporated, A. G., "STK/SEET Geomagnetic Field Graphics," Satellite Tool Kit Application Help.
34. Singer, H., Southwood, D., Walker, R., and Kivelson, M., "Alfven Wave Resonances in a Realistic Magnetospheric Magnetic Field Geometry," *Journal of Geophysical Research*, Vol. 86, No. A6, 1981, pp. 4589–4596.
35. Bass, J. and Jordan, C., "Models of the External Source Contribution to Magnetospheric Magnetic Fields for CRRES Data Analysis," <http://www.dtic.mil/dtic/tr/fulltext/u2/a221059.pdf>, 1990, [Online; Accessed 25-November-2011].
36. Pramoda, K. e. a., "Square Loop Coil System for Balancing and Calibration of Second-Order SQUID Gradiometers," *Journal of Physics: Conference Series* 208, 2010.
37. Agency, E. S., "Magnetic Coil Facility at ESTEC," <http://sci.esa.int/science-e/www/object/index.cfm?fobjectid=45846>, 2009, [Online; Accessed 20-Oct-2011].
38. Poppenk, F M, A. R. and Brouwer, G. F., "Design and Application of a Helmholtz Cage for Testing Nano-Satellites," Noordwijk, The Netherlands, 2007.
39. AlphaLab, I., "DC Milligauss Meter 3 Axis," <http://www.trifield.com/content/dc-milligauss-meter-3-axis/>, [Online; Accessed 22-Sept-2011].
40. National Test Equipment, I., "Power Supply Product Pages," <http://www.nationaltestequipment.com>, 2011, [Online; Accessed 23-Dec-2011].
41. Honeywell, "Smart Digital Magnetometer HMR2300," <http://www.honeywell.com/magneticsensors>, 2006, [Online; Accessed 23-Dec-2011].
42. Springmann, J., Cutler, J., and Bahcivan, H., "Magnetic Sensor Calibration and Residual Dipole Characterization for Application to Nanosatellites," Toronto, Ontario Canada, 2010, August 2010.
43. Wiesel, W., *Spaceflight Dynamics, 3rd Ed.*, Aphelion Press, 2010.

44. Hall, C., "Chapter 3 Kinematics," <http://www.dept.aoe.vt.edu/~cdhall/courses/aoe4140/>, 2003, [Online Lecture Notes; Accessed 6 Jan 2012].
45. Schuster, M., "A Survey of Attitude Representations," *The Journal of the Astronautical Sciences*, Vol. 41, No. 4, 1993, pp. 439–517.
46. Shuster, M., "The Generalized Wahba Problem," *Journal of the Astronautical Sciences*, Vol. 54, No. 2, 2006, pp. 245–259.
47. Anderson, A.D., S. J. and Hashida, Y., "Attitude Determination and Control System Simulation and Analysis for Low-Cost Micro-satellites," 2004 IEEE, March 2004.
48. Kirk, D., *Optimal Control Theory: An Introduction*, Dover, 1998.
49. Bryson, A., *Dynamic Optimization*, Addison-Wesley, 1999.
50. Euripides, P., "Square Helmholtz Coils Demonstration," <http://demonstrations.wolfram.com/SquareHelmholtzCoils/>, [Online; Accessed 11-Oct-2011].
51. Users, M., "HMC5843 Lib Update," <http://www.arduino.cc/cgi-bin/yabb2/YaBB.pl?num=1274748346>, 2010, [Online; Accessed 8-Jan-2012].
52. Padro, J., *Development of a Star Tracker-based Reference System for Accurate Attitude Determination of a Simulated Spacecraft*, Master's thesis, Graduate School of Engineering and Management, Air Force Institute of Technology (AU), Wright-Patterson AFB OH, 2012.
53. Cobb, R., "Vibration Damping and Control - Smart Materials & Smart Structures Part I," Mech 719 Lecture Notes, 2011.

REPORT DOCUMENTATION PAGE			<i>Form Approved</i> <i>OMB No. 0704-0188</i>	
<p>The public reporting burden for this collection of information is estimated to average 1 hour per response, including the time for reviewing instructions, searching existing data sources, gathering and maintaining the data needed, and completing and reviewing the collection of information. Send comments regarding this burden estimate or any other aspect of this collection of information, including suggestions for reducing this burden to Department of Defense, Washington Headquarters Services, Directorate for Information Operations and Reports (0704-0188), 1215 Jefferson Davis Highway, Suite 1204, Arlington, VA 22202-4302. Respondents should be aware that notwithstanding any other provision of law, no person shall be subject to any penalty for failing to comply with a collection of information if it does not display a currently valid OMB control number. PLEASE DO NOT RETURN YOUR FORM TO THE ABOVE ADDRESS.</p>				
1. REPORT DATE (DD-MM-YYYY) 22-03-2012		2. REPORT TYPE Master's Thesis		3. DATES COVERED (From — To) Aug 2011 – Mar 2012
4. TITLE AND SUBTITLE CubeSat Attitude Determination and Helmholtz Cage Design			5a. CONTRACT NUMBER	
			5b. GRANT NUMBER	
			5c. PROGRAM ELEMENT NUMBER	
6. AUTHOR(S) Brewer, Megan R., Capt, USAF			5d. PROJECT NUMBER	
			5e. TASK NUMBER	
			5f. WORK UNIT NUMBER	
7. PERFORMING ORGANIZATION NAME(S) AND ADDRESS(ES) Air Force Institute of Technology Graduate School of Engineering and Management (AFIT/ENY) 2950 Hobson Way WPAFB OH 45433-7765			8. PERFORMING ORGANIZATION REPORT NUMBER AFIT/GAE/ENY/12-M03	
9. SPONSORING / MONITORING AGENCY NAME(S) AND ADDRESS(ES) Intentionally left blank			10. SPONSOR/MONITOR'S ACRONYM(S)	
			11. SPONSOR/MONITOR'S REPORT NUMBER(S)	
12. DISTRIBUTION / AVAILABILITY STATEMENT APPROVED FOR PUBLIC RELEASE; DISTRIBUTION UNLIMITED				
13. SUPPLEMENTARY NOTES This material is declared a work of the U.S. Government and is not subject to copyright protection in the United States.				
14. ABSTRACT A method of 3-axis satellite attitude determination utilizing six body-fixed light sensors and a 3-axis magnetometer is analyzed. A Helmholtz cage is designed, built, and tested to provide a dynamic, 3-axis, uniform magnetic field to cancel the Earth's magnetic field and create an environment similar to the geomagnetic field a satellite would experience on-orbit. A CubeSat is provided the inertial magnetic vector and ``Sun" vector which are combined with data from the light sensors and magnetometer in a CubeSat. Attitude is estimated on-board the CubeSat via the optimal fast quaternion estimation algorithm. The capabilities of the Helmholtz cage including the uniformity of the produced magnetic field are examined as well as the accuracy of the on-board attitude determination. The results show that a support column in the vicinity of the cage impacts the uniformity of the magnetic field. The desired +/- 2 Gauss magnetic field was achieved in two of three directions and the cage is equipped to simulate a dynamic magnetic field as would be experienced in orbit. Attitude determination with the OFQEA is achieved to within +/- 6° of error.				
15. SUBJECT TERMS Attitude Determination, CubeSat, Helmholtz Cage				
16. SECURITY CLASSIFICATION OF:			17. LIMITATION OF ABSTRACT UU	18. NUMBER OF PAGES
a. REPORT U	b. ABSTRACT U	c. THIS PAGE U		
			19a. NAME OF RESPONSIBLE PERSON Dr. Eric. D. Swenson	
			19b. TELEPHONE NUMBER (Include Area Code) (937)255-3636, ext 7479 Email: Eric.Swenson@afit.edu	